Marine Geology 435 (2021) 106453

Contents lists available at ScienceDirect

Marine Geology

journal homepage: www.elsevier.com/locate/margo

Research article

A 100-km wide slump along the upper slope of the Canadian Arctic was likely preconditioned for failure by brackish pore water flushing

C.K. Paull [a,*], S.R. Dallimore [b], D.W. Caress [a], R. Gwiazda [a], E. Lundsten [a], K. Anderson [a], H. Melling [c], Y.K. Jin [d], M.J. Duchesne [e], S.-G. Kang [d], S. Kim [d], M. Riedel [f], E.L. King [g], T. Lorenson [h]

[a] Monterey Bay Aquarium Research Institute, Moss Landing, CA, USA
[b] Geological Survey of Canada, Sidney, BC, Canada
[c] Fisheries and Oceans Canada, Sidney, BC, Canada
[d] Korea Polar Research Institute, Incheon, South Korea
[e] Geological Survey of Canada, QC, Canada
[f] GeoMar, Kiel, Germany
[g] Geological Survey of Canada, Dartmouth, Canada
[h] U.S. Geological Survey, Santa Cruz, CA, USA

ARTICLE INFO

Keywords:
Submarine slope failures
Continental margin morphology
Cold venting process and products
Arctic Ocean
Autonomous Underwater Vehicles

ABSTRACT

Exploration of the continental slope of the Canadian Beaufort Sea has revealed a remarkable coalescence of slide scars with headwalls between 130 and 1100 m water depth (mwd). With increased depth, the scars widen and merge into one gigantic regional slide scar that is more than 100 km wide below ~1100 mwd. To understand the development of these features, five sites were investigated with an Autonomous Underwater Vehicle, which provided 1-m bathymetric grids and Chirp profiles, and surveyed with a Remotely Operated Vehicle. The morphologies are consistent with retrograde failures that occurred on failure planes located between 30 and 75 m below the modern seafloor. At issue is whether the continental slope in this area is preconditioned for failure. While rapid sedimentation during glacial periods, and the presence of shallow gas cannot be ruled out, given the geological environment, it is unclear that they are primary preconditioning factors. Evidence of widespread flushing of the slope with brackish waters, and observed flows of brackish water within slide scars, suggest fluid venting and overpressure may play a role in the development of the extensive slope failures seen along this margin. The impact of pore water salinity changes at the depth of the failure plane on slope stability has not been considered in marine settings previously.

1. Introduction

Scars left by submarine slope failures are particularly common along the continental slopes of passive margins (e.g., Hampton et al., 1996; Weaver et al., 2000; Piper and McCall, 2003; Dugan and Flemings, 2000; Huhnerbach and Masson, 2004; Masson et al., 2006; Twichell et al., 2009; Talling et al., 2014). Many factors can contribute to these failures, including rapid deposition and the build-up of excess pore pressure at depth (e.g., Locat, 2001; Locat and Lee, 2002; Masson et al., 2010). Failures can be facilitated by weak layers at depth (Locat et al., 2014) or where interstitial gas bubbles are present within the sediment matrix (Paull et al., 2000). Areas with thick sections of rapidly deposited sediments are especially prone to failures (Twichell et al., 2009). This study provides detailed documentation of parts of large slide scars that occur on the slope of the Canadian Beaufort Sea, offshore of the Northwest Territories, Canada (Fig. 1), using state-of-the-art survey tools. The goal of this study is to evaluate whether the massive seafloor morphological features observed on the slope are due to the unique conditions along this margin, which precondition the seafloor for deformation and/or failure. In particular, we evaluate whether the propensity for slope failure may be related to relict permafrost occurrence in the adjacent shelf, and presence of brackish pore waters within the slope sediments.

* Corresponding author.
E-mail address: paull@mbari.org (C.K. Paull).

https://doi.org/10.1016/j.margeo.2021.106453
Received 6 April 2020; Received in revised form 10 February 2021; Accepted 12 February 2021
Available online 18 February 2021

1.1. Geological setting

Regional assessment of the subsurface geology of the Canadian Beaufort Sea suggests the area (Fig. 1) is underlain by a seaward thickening wedge of post-Cretaceous sediments that reach more than 10 km in thickness (Dietrich et al., 1985; Dixon et al., 2019). More than 100 hydrocarbon exploration wells drilled on the shelf provide information about the stratigraphy of the subsurface sediments, permafrost and gas hydrate occurrences, and anomalous overpressure (Siddiqui, 1988; Osadetz and Chen, 2010; Hu et al., 2013, 2018). Observations from wells drilled in mid-shelf locations suggest that the Quaternary section can be up to a kilometer-thick and is comprised of a succession of transgressive/regressive deposits (Blasco et al., 1990) thought to reflect sea level changes during Pleistocene glaciations.

A well-defined morphologic break occurs in the Canadian Beaufort Sea at approximately 110 m water depth (mwd) which separates the Beaufort Shelf from the upper slope (Figs. 1 and 2). The subsurface sediments beneath the upper slope are complexly bedded with several intervals displaying wavy and contorted reflection packages of variable amplitudes characteristic of mass-transport deposits (Sun et al., 2017), which are commonly seen along this margin (Mosher et al., 2012; Mosher and Hutchinson, 2019).

The first systematic multibeam surveys of the outer shelf and upper slope of the Canadian Beaufort Sea were gathered in 2009 under the auspices of an industry-academic consortium, ArcticNet (http://www.omg.unb.ca/Projects/Arctic/google/). The surveys revealed a number of geomorphic features that have potential geohazard implications. Initial attention was focused on a 22 km-wide slide scar that extends up to near the present shelf edge. It has a sharp morphologic expression (Fig. 1; Mosher, 2009; Saint-Ange et al., 2014) suggesting that it is the result of a recent failure. This large slide is part of slide complexes that occur between the US/Canadian border and the mouth of Amundsen Gulf, as identified in bathymetric and sub-bottom profiler data, with run-outs exceeding 130 km (Blasco et al., 2013; Cameron and King, 2019; Mosher and Hutchinson, 2019). The multibeam bathymetry also showed mud volcanoes occurring sporadically along the slope, which may indicate overpressured conditions at depth (Paull et al., 2015a).

1.2. Glacial and permafrost history

The outer shelf edge of the Canadian Beaufort Sea was not extensively ice covered during the last glaciation (Dyke, 2004; England et al., 2009). However, ice streams flowing north through the Mackenzie Trough and west out of Amundsen Gulf (Batchelor et al., 2013; Jakobsson et al., 2014, Keigwin et al., 2018; Klotsko et al., 2019; Fig. 1) presumably provided large volumes of sediments to the slope.

During the glacial sea level low stands the exposed Arctic shelf experienced very cold mean annual surface temperatures (<−20 °C), which resulted in substantial permafrost formation. Exploration wells document that the Quaternary shelf sediments still contain relict permafrost down to 700 m below seafloor (mbsf) (Weaver and Stewart, 1982; Pelletier, 1988). The relict permafrost is inferred to extend out to near the shelf edge (Taylor et al., 2014; Frederick and Buffett, 2015; Pelletier, 1988; Blasco et al., 2013).

The last postglacial marine transgression imposed a large thermal change on shelf sediments as bottom water temperatures are always ≥ −1.8 °C, the freezing point for sea water. This thermal disturbance is still propagating into the subsurface (Taylor et al., 2014), stimulating the decomposition of submerged terrestrial permafrost and gas hydrate at depth (Weaver and Stewart, 1982; Riedel et al., 2017). These processes can result in significant sediment property changes through the release of pore water and methane, the reduction of sediment strength, and in some instances the creation of overpressure.

Early researchers recognized that areas of the Beaufort Shelf underlain by relict permafrost had a number of unique seafloor features. The name pingo-like-feature (PLF) was used to describe isolated submarine circular topographic highs which are up to 100 m in diameter and stand up to 40 m in height with respect to the surrounding nearly flat seafloor on the shelf (Shearer et al., 1971; Pelletier, 1988). PLFs are similar in size and shape to terrestrial pingos observed along the Arctic coastal plain (i.e., Mackay, 1998). The positive relief of terrestrial pingos is attributed to the expansion associated with ground ice formation and the larger pingos are connected to open hydrologic systems, which provide additional waters from below. Sediment coring at several PLFs shows that shallow sediments within PLFs are frozen and contain visible ice (Yorath et al., 1971; Poley, 1982; Paull et al., 2007; Gwiazda et al., 2018).

Chloride measurements on pore waters extracted from over a hundred sediment cores collected on the Beaufort Shelf and slope show downcore freshening is widespread, especially on the upper slope near the shelf edge (Paull et al., 2015a; Gwiazda et al., 2018). Apparently fresh waters have pervasively been infused into slope sediments. The present seawater column of the Canadian Beaufort Sea is stratified with an intermediate layer of cold water (i.e., temperatures as low as −1.5 °C) extending from the base of the seasonal thermocline (> ~ 30 m) down to ~200 mwd (McLaughlin et al., 2004; Melling, 1998). The unusual hydrography sets the conditions for brackish water to freeze within seafloor sediment in a zone between 30 and 200 mwd.

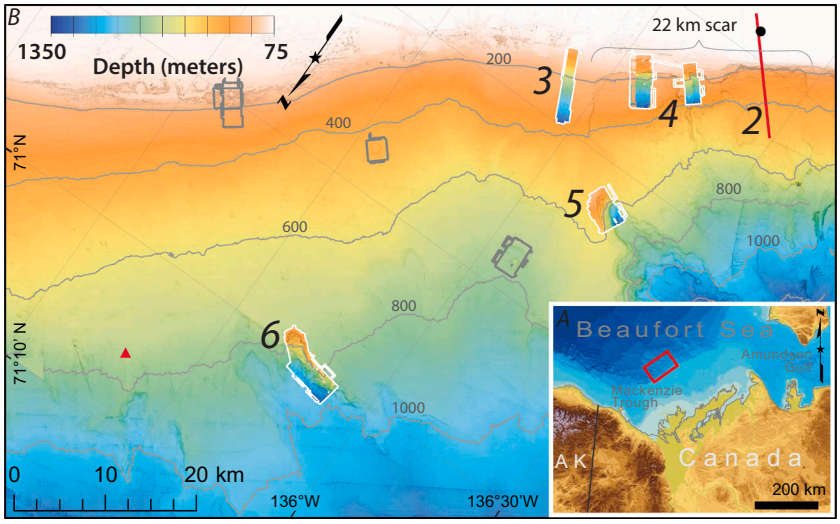

Fig. 1. Maps showing locations of AUV surveys with respect to the morphology of the continental slope along the Canadian Beaufort Sea. Location of the study area (B) is indicated in A (red box). Bathymetric map in B based on the ArcticNet multibeam surveys show AUV mapping surveys presented in Figs. 3 to 6 outlined in white (10.26022/IEDA/330047). Red line indicates location of multichannel seismic profile shown in Fig. 2. Red triangle indicates location of core JPC15 of Klotsko et al. (2019). Areas mapped in published AUV surveys concerning mud volcanoes (Paull et al., 2015a) and shelf edge PLFs (Paull et al., 2019) are outlined in grey. Contours are at 200 m intervals. The 22 km-wide slide scar which reaches the uppermost slope is indicated. Slide scars merge downslope and coalesce into one giant slide scar. (For interpretation of the references to colour in this figure legend, the reader is referred to the web version of this article.)

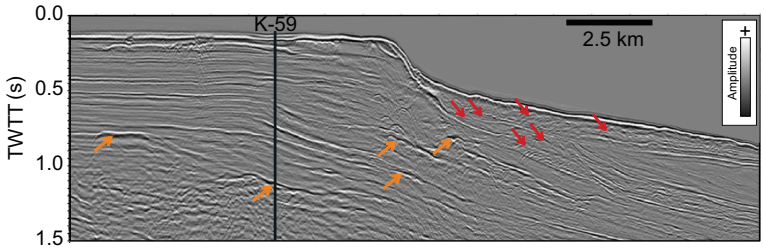

Fig. 2. Multichannel seismic profile (*R/V Araon* cruise ARA05C line 8) extending from the outer shelf to the upper continental slope of the 22 km-long slide scar uppermost slope of the Beaufort Sea (Jin et al., 2015). Profile location indicated by red line in Fig. 1. Red arrows - mass transport deposits; Orange arrows - amplitude anomalies. Black vertical line is Nektoralik K-59 well (Hu et al., 2013, 2018). (For interpretation of the references to colour in this figure legend, the reader is referred to the web version of this article.)

2. Methods

The Geological Survey of Canada (GSC), Fisheries and Oceans Canada, and the Monterey Bay Aquarium Research Institute (MBARI) have jointly conducted five cruises on the Canadian Coast Guard icebreaker *Sir Wilfrid Laurier* in 2003 (WL03; Paull et al., 2007), 2010 (2010–035-WD; Paull et al., 2011), 2012 (2012004PGC), 2013 (2013005PGC; Paull et al., 2015a), and 2016 (Gwiazda et al., 2018) to study the marine geology of the Canadian Beaufort Sea shelf and slope. The Korean Polar Research Institute (KOPRI) joined this collaboration, conducting cruises on the South Korean icebreaker *Araon* in 2013 (ARA04C, Jin et al., 2015), 2014 (ARA05C, Paull et al., 2015a; Jin and Dallimore, 2016), and 2017 (ARA08C). Here we present seafloor surveys conducted in five areas (Fig. 1) using an Autonomous Underwater Vehicle (AUV) configured for seafloor mapping (Caress et al., 2008), supplemented with Remotely Operated Vehicle (ROV) observations made during these cruises.

2.1. AUV Mapping surveys

Detailed mapping surveys were conducted at four sites along the uppermost slope which show progressively increasing seafloor deformation downslope. These include an AUV dive on the *Gentle Shelf- Slope Transition* (Fig. 3), a dive at *Shelf Edge Scar with Staircase of Terraces in > 130 mwd* (Fig. 4), and a dive on the *Shelf Edge Scar with Adjacent Remnant Section in > 141 mwd* (Fig. 4). AUV surveys also covered two slide scar areas on the slope which do not extend up to the present shelf edge: with two dives on *Scar with Headwall in > 519 mwd* (Fig. 5), and two dives in the *Scar with Headwall in > 715 mwd* (Fig. 6). During these mapping cruises three other areas were surveyed, which have been reported on elsewhere (Fig. 1; Paull et al., 2015a, 2019).

The AUV(s) carried a Reson 7125, 200-kHz multibeam sonar in 2013 and 2016, a Reson 7125, 400-kHz in 2017, and an Edgetech 1- to 6-kHz Chirp sub-bottom profiler on all the surveys. The AUVs were pre-programmed to proceed to >50 waypoints while traveling at 3 knots and maintaining an altitude of 50 m off the seafloor. During each dive up to 9 km^2 were surveyed with ~150 m spaced tracklines. In this mode, overlapping multibeam bathymetric coverage is obtained at a vertical resolution of 0.15 m and at a horizontal resolution of 0.87 m, whereas Chirp seismic-reflection profiles are produced at a vertical resolution of 0.11 m. Initial navigation fixes are obtained from Global Positioning System when the AUV is at the sea surface and subsequently updated with a Kearfott inertial navigation system and a Doppler velocity log when within 100 m of the seafloor. Data processing was done using the open source software package MB-System (Caress and Chayes, 1996; Caress et al., 2008).

2.2. ROV dives

Ground truth observations were made on 17 ROV dives within five of the AUV survey areas conducted in 2012, 2013, 2016, and 2017. The MBARI-built ROV carried an Insite Nova Camera, a Falmouth Scientific Instruments Micro CTD, and an Imagenex Technology (Model 881A) obstacle avoidance sonar. A mechanical arm to collect solid material (i.e., cobbles) was added for the 2013 dives. In 2016, the ability to collect 20-cm long push cores was added and four push cores were extruded and sectioned into 1-cm slices on shipboard. ^{210}Pb activities were measured

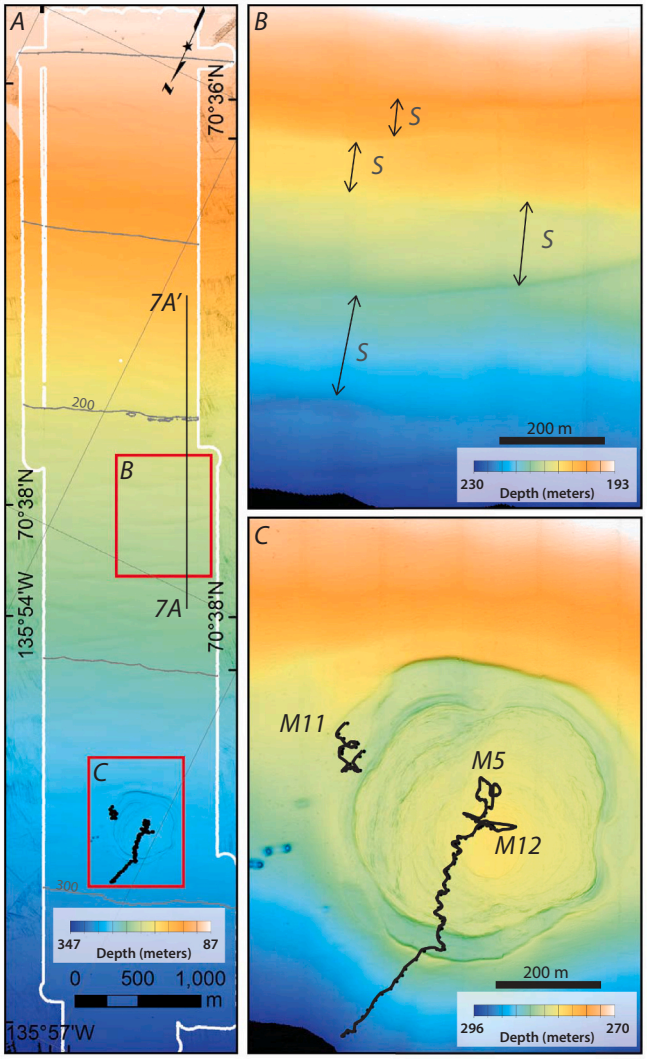

Fig. 3. Maps showing bathymetry derived from *Gentle Shelf-Slope Transition* AUV survey (10.26022/IEDA/329971). Bathymetry is rotated such that the shelf edge is parallel to the top of the page.
Location of survey indicated in Fig. 1. Area outlined in white in A shows the entire AUV survey superimposed on a regional multibeam grid with 50 m contours in grey. Red squares are areas illustrated in B and C in more detail. Straight black line 7A-7A' is the location of the Chirp profile segment shown in Fig. 7. B shows the subtle contour-parallel swales (S). C shows top of a mud volcano and ROV dive transects M5, M11, and M12 (thick black lines) discussed in Paull et al. (2015a), (For interpretation of the references to colour in this figure legend, the reader is referred to the web version of this article.)

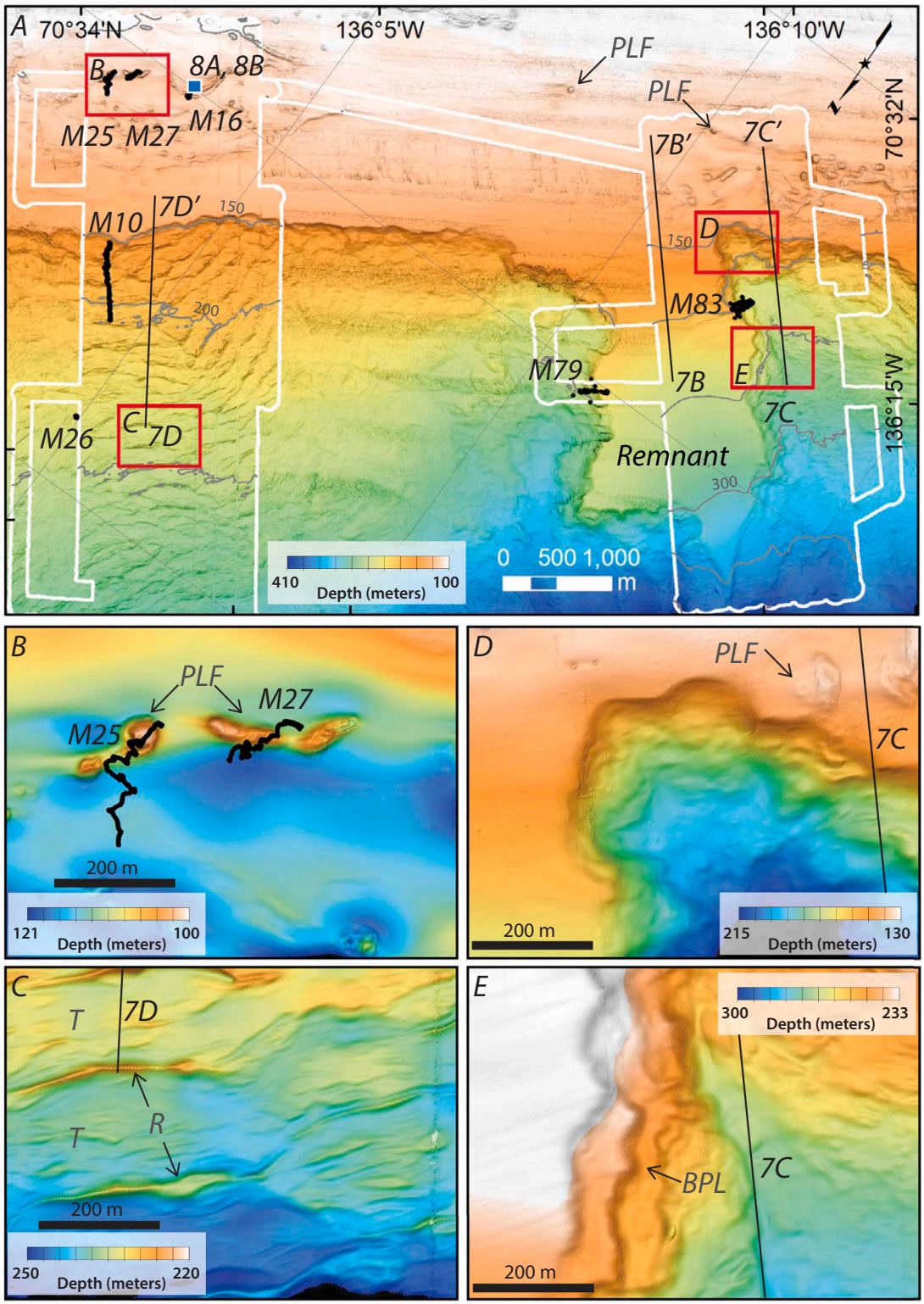

Fig. 4. Map showing bathymetry of sites *Shelf Edge Scar with Staircase of Terraces in > 130 mwd* (10.26022/IEDA/329965) and *Shelf Edge Scar with Adjacent Remnant Section in > 141 mwd* (10.26022/IEDA/329966). Bathymetry was rotated such that the shelf edge is parallel to the top of the page.
Location of surveys indicated in Fig. 1. Area outlined in white in A shows entire AUV survey superimposed on a regional multibeam grid with 50 m contours in grey. Red squares are areas illustrated in B, C, D, and E in more detail. Straight black lines are location of Chirp profile segments 7B-7B', 7C-7C', and 7D-7D' shown in Fig. 7. Blue squares are the locations of photos and samples shown in Fig. 8A and B. Thick black lines indicate locations of ROV dives M10, M16, M25, M26, M27, M79 and M83. Locations of pingo-like-features (PLF), distinctive terrace edge ridges (R), terraces (T) and bedding plane ledges (BPL) are indicated. (For interpretation of the references to colour in this figure legend, the reader is referred to the web version of this article.)

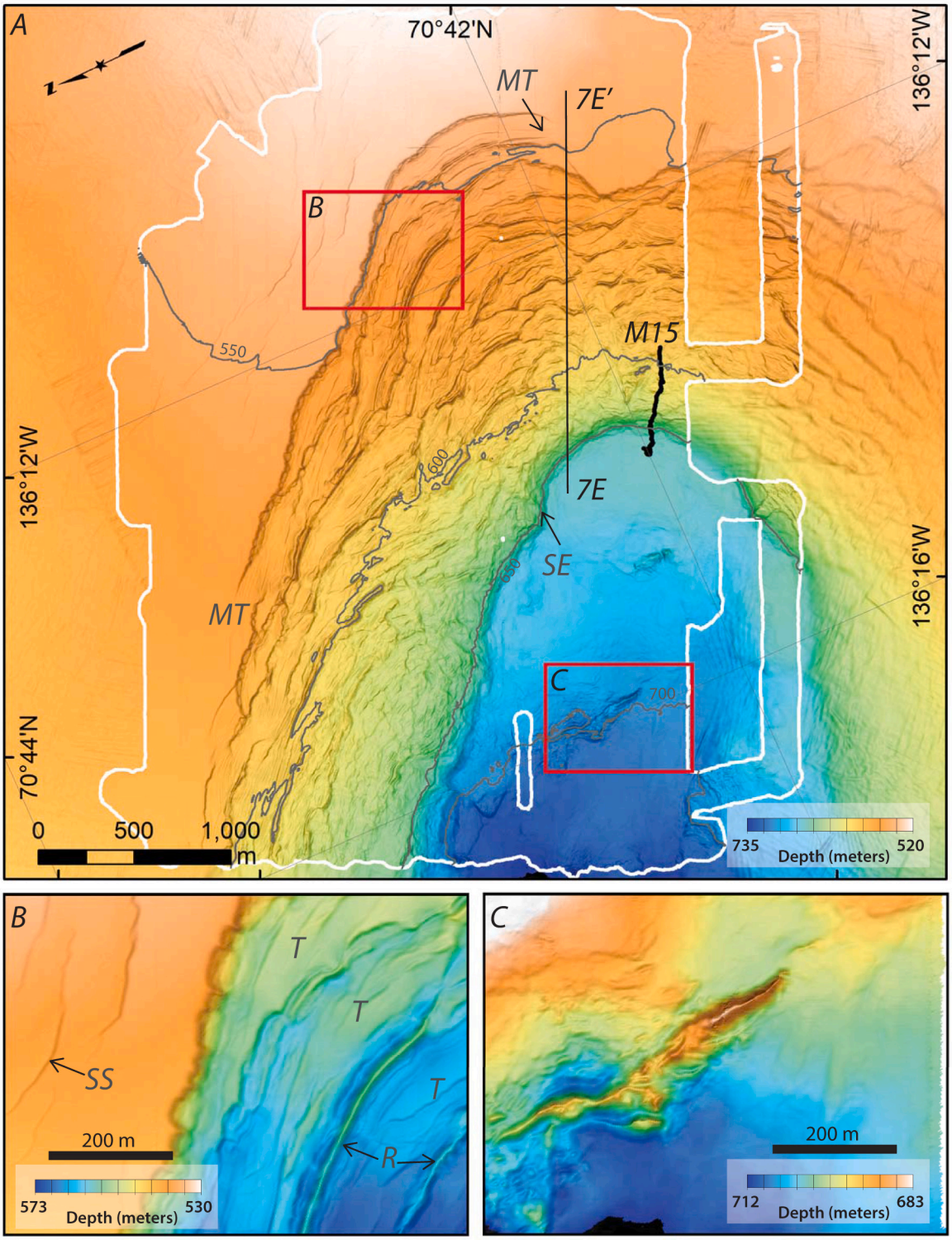

Fig. 5. Map showing bathymetry of *Scar with Headwall in > 519 mwd* site (10.26022/IEDA/329967, 10.26022/IEDA/329970).
Bathymetry is rotated such that the shelf edge is parallel to the top of the page. Location of survey indicated in Fig. 1. Area outlined in white in A shows AUV survey superimposed on a regional multibeam grid with 50 m contours in grey. Red squares are areas illustrated in B, and C in more detail. Straight black line 7E - 7E' shows location of Chirp profile segment presented in Fig. 7. Locations of ROV dive transect (thick black line), secondary escarpment (SE), small scarps (SS), terraces (T), merged terrace (MT), and distinctive terrace edge ridges (R) are indicated. (For interpretation of the references to colour in this figure legend, the reader is referred to the web version of this article.)

at the US Geological Survey in Santa Cruz, California, following techniques of Swarzenski et al., 2006. In 2016 a thermal probe with a 0.01 °C resolution was mounted on the side of the mechanical arm which could be inserted up to 20 cm into the sediment. The composition of selected sediment samples was analyzed with a scanning electron microscope equipped with energy dispersive X-ray (EDX-SEM) at the Moss Landing Marine Lab, California State University.

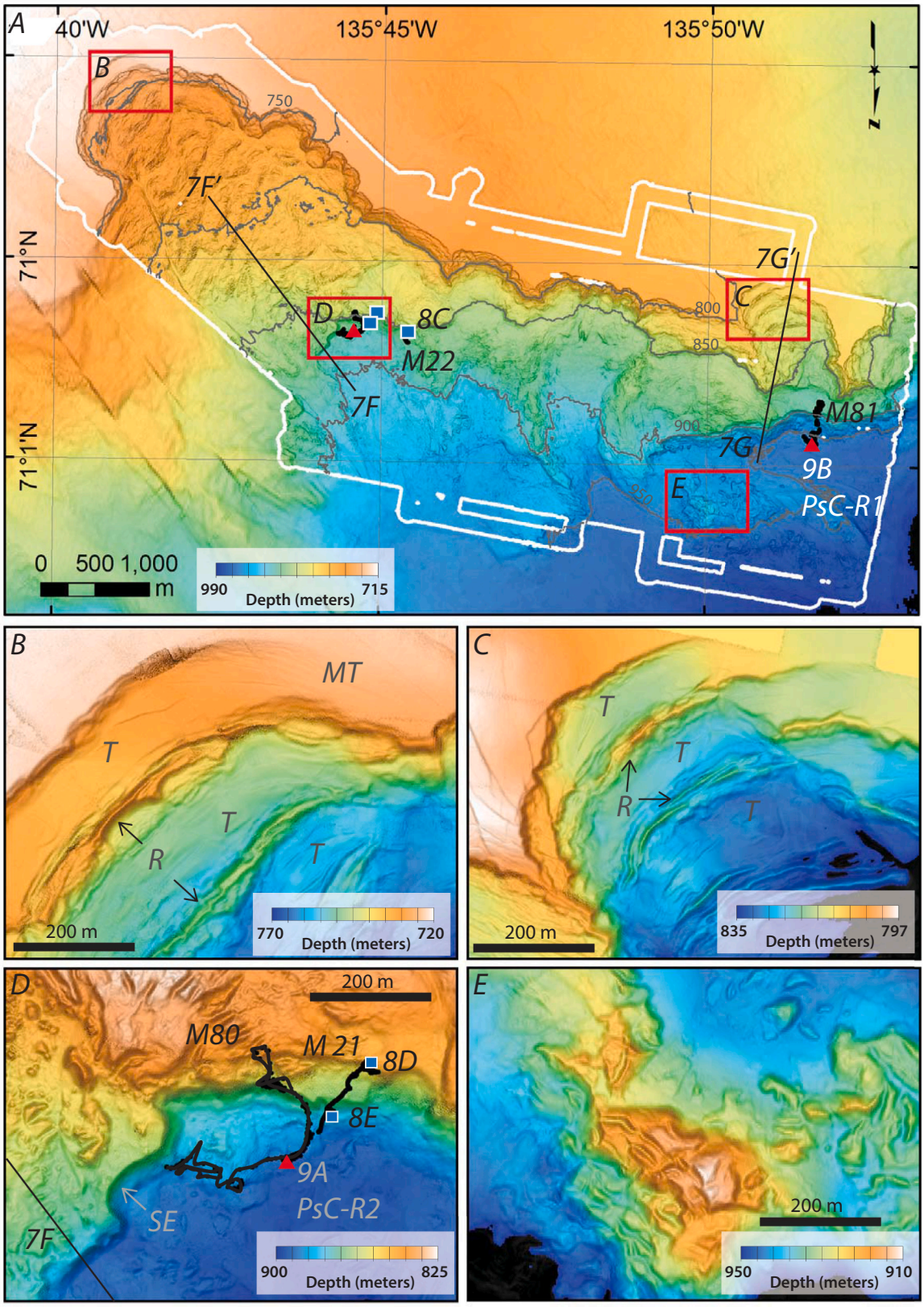

Fig. 6. Maps showing bathymetry derived from *Scar with Headwall in > 715 mwd* AUV survey (10.26022/IEDA/329968, 10.26022/IEDA/329969). Location of survey indicated in Fig. 1. Bathymetry is rotated to fit the page. Area outlined in white in A shows AUV survey superimposed on a regional multibeam grid with 50 m contours in grey. Red squares are areas illustrated in B, C, D, and E in more detail. Straight black line shows location of Chirp profile segments 7F–7F' and 7G–7G' shown in Fig. 7. Blue squares indicate location of photos and samples shown in Fig. 8C, D, and E. Thick black lines in A and D show locations of ROV dives transects. Red triangles are the locations of push cores with ^{210}Pb measurements shown in Fig. 9. Secondary escarpment (SE), distinctive terrace edge ridge (R), terraces (T), and merged terrace (MT) are indicated. (For interpretation of the references to colour in this figure legend, the reader is referred to the web version of this article.)

3. Results

3.1. AUV surveys

The AUV surveys provide an opportunity to examine in detail the morphology of the shelf edge and upper slope (Fig. 1). In the following section, we present results from AUV surveys of one site with a relatively undisturbed transition from shelf to slope, two sites along an extensive failure scar that extends up to near the shelf edge, and two sites along the headwalls of deep-water failure scars.

3.1.1. Gentle shelf-slope transition

A 1.2 km-wide corridor between 87 and 346 mwd was surveyed where the shelf-slope transition morphology is relatively undisturbed (Figs. 1 and 3A). Below 100 mwd the bottom is smooth with an average slope of 1.7°. The resolution of the AUV surveys reveals subtle contour-parallel linear swales on this surface (S - Fig. 3B). These features have ≤ 50 cm amplitudes and 50 to 250 m wavelengths. The survey extended 8.2 km downslope to include the top of a mud volcano in 281 mwd (Fig. 3C; Paull et al., 2015a). Chirp profiles of the upper ~40 ms Two Way Travel (TWT; ~30 m) below the seafloor show finely layered and laterally continuous reflectors that are nearly parallel to the seafloor (LS - Fig. 7A). A similar acoustic signature consisting of numerous laterally continuous reflectors over a seismically homogeneous unit is characteristic of the slope regionally (Saint-Ange et al., 2014; Klotsko et al., 2019). In ≥ 120 mwd, Chirp profiles show disrupted strata in the troughs separating the swales (SD - Fig. 7A).

3.1.2. Shelf edge scar with staircase of terraces in > 130 mwd

A section of the 22 km-wide escarpment identified in the regional surface ship multibeam bathymetry (Mosher, 2009; Saint-Ange et al., 2014) between 85 and 322 mwd was surveyed (Figs. 1 and 4). Here the escarpment initiates at 130 to 144 mwd, has slopes of ≥ 15°, and ~ 30 m of relief.

Immediately above the escarpment there is a 420 to 750 m wide zone of comparatively smooth seafloor with a seaward slope of 1.2° (Fig. 4) composed of layered sediments (LS - Fig. 7D). Chirp profiles show that acoustic blanking is present within the PLF-rich zone (PLF - Fig. 4B), but does not occur within the ≥ 420 m wide band between the PLF-rich zone and the escarpment (AB - Fig. 7D).

Below the headwall scarp is a distinctive morphology composed of a staircase of tilted terraces that are 100 to 250 m across (T - Fig. 4C). Chirp profiles show the terraces are rotated blocks of layered sediment, which in places dip toward the shelf edge at up to 15° (RB - Fig. 7D). On the outer edges of many terraces are several ≥ 100 m long ridges that are ≤ 4 m high and ≤ 35 m wide (T, R - Fig. 4C). The offset between the layered sediment on adjacent blocks indicates ~40 m of throw is common on the faults that separate the rotated blocks (RB - Fig. 7D). Chirp profiles do not show a discernible drape of post-failure hemipelagic sediment.

3.1.3. Shelf edge scar with adjacent remnant section in > 141 mwd

Another section of the 22 km-wide headwall scarp covered in Section 3.1.2 but farther to the west, was also surveyed (Figs. 1 and 4). It covers an area between 99 and 410 mwd that includes the western half of a tongue-shaped ridge, the adjacent headwall scarp, and some of the floor inside the slide scar (Figs. 1 and 4). This ridge appears to be an intact

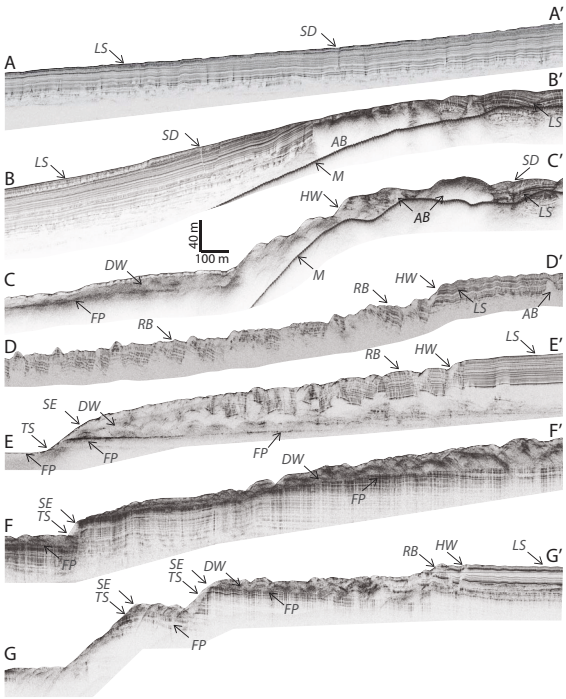

Fig. 7. Chirp sub-bottom profile dip lines showing the character, deformation and failure along shelf edge (A-D) and slope (A-G). Locations of profiles are indicated in Figs. 3-6. LS- layered sediments, SD- stratal disruptions, M- multiple reflection from surface echo, HW- headwall scarp, SE – secondary escarpment, AB- blanking, RB- rotated blocks, FP- failure plane, DW- debris wedge, TS- truncated strata. Vertical scale bar assumes 1500 m/s sound velocity (10.26022/IEDA/329996, 10.26022/IEDA/329997, 10.26022/IEDA/329998, 10.26022/IEDA/329999, 10.26022/IEDA/330000, 10.26022/IEDA/330001, 10.26022/IEDA/330002, 10.26022/IEDA/330003).

remnant of the upper slope. Below 350 mwd the scars on both sides of the remnant feature merge.

A change in the seafloor slope and texture occurs at 135 to 150 mbsf on the surface of the intact remnant. The average slopes increase from ~1.2° to ~3.2° at 135 mwd (Fig. 4A). The seafloor texture is characterized by rough topography associated with PLFs (PLF - Fig. 4A and D) and underlying acoustic blanking (AB - Fig. 7B) and a generally smooth surface topography with subsurface layered sediment under the remnant section below.

Superimposed on the smooth seafloor surface of the intact remnant seafloor are subtle contour-parallel linear swales, which are up to 0.50 m in amplitude, spaced at 25 to 70 m apart. Chirp profiles across the remnant below 150 mwd show a ~ 65 ms TWT (~49 m) thick zone with numerous reflections that are nearly parallel to the seafloor (LS - Fig. 7B). Ledges on the side of the remnant seafloor block reflect truncated bedding (BPL - Fig. 4E).

The semicircular headwall scarp to the west of the remnant seafloor area between 141 and 236 mwd has an average slope of 8.5° (Fig. 4D). This is the only place where the headwall cuts into sediments associated with the band of shelf edge pingos (PLF - Fig. 4A, B, and D) and seismic blanking (HW, AB - Fig. 7C). The surface of the slide below 236 mwd slopes at ~1.2°. Chirp profiles across the floor of the slide show a > 30-m thick mass of acoustically homogenous wedge of debris bound at its lower base by a continuous acoustically diffuse but more reflective plane (DW, FP - Fig. 7C). It thins further downslope, suggesting that this reflector represents the failure surface. Chirp profiles do not show a discernible drape of post-failure hemipelagic sediment.

3.1.4. Scar with headwall in > 519 mwd

The AUV survey covered the northern side of a semicircular headwall scarp in 519 to 736 mwd. The regional multibeam bathymetry shows this scar is entirely confined to the slope (Figs. 1 and 5) and merges with the much larger regional scar below ~1100 mwd.

Above the main headwall scarp, a smooth seafloor surface slopes at ~1.3°, consistent with the slope of unfailed areas regionally. Here, Chirp profiles show the upper ~40 ms TWT (~30 m) is composed of laterally continuous parallel reflectors (LS - Fig. 7E). Below this thin acoustic layering a few faint seafloor-parallel reflectors occur down at 120 ms TWT (~90 mbsf). On the northeast side and above the headwall, there are ~600 m long fault scarps (crown cracks) with ≤ 1.5 m of relief oriented subparallel to the headwall (SS - Fig. 5B).

Below the main headwall scarp (≥ 532 mwd), there is a ≥ 1100 m wide zone sloping at ~2.9°, and composed of a staircase of 50 to 100 m wide terraces that wrap around the scar (T - Fig. 5B). The edge of the uppermost terrace merges laterally with the undeformed slope sediments regionally (MT - Fig. 5A). In Chirp profiles these terraces are the tops of fault-bounded rotated blocks (RB - Fig. 7E). The reflection pattern within the rotated blocks nearest to the headwall is indistinguishable from the undeformed sediment upslope. The outer edges of the terraces have distinctive linear ridges that are commonly over 200 m long, ≤ 5 m high and ≤ 30 m wide (T, R - Fig. 5B). The integrity of the terraces decreases downslope leaving only broken vestiges of the terrace-edge ridges.

In ≥ 635 mwd within the main scar there is a conspicuous ~25 m high, ~20° sloping, semicircular, secondary escarpment (SE - Fig. 5). Chirp data show a strong laterally continuous reflection, truncated at the face of this secondary escarpment (FP, SE - Fig. 7E), that has a slope of ~1.3° consistent with the regional dip outside of the scar. Chaotic reflections and deformed strata overly this reflection which are taken to be a debris wedge overlying the failure plane (DW, FP - Fig. 7E). Upslope projection of the deep reflector positions it at ~75 mbsf with respect to the top of main headwall.

Below the semicircular secondary escarpment (> 660 mwd) a few huge pieces of talus, including a ~ 550 m long feature (Fig. 5C) with a shape similar to the linear ridges on the edges of the terraces above (T - Fig. 5B), lie on this surface. Otherwise the bottom is lacking a noticeable cover of debris and in Chirp profiles the seafloor forms a strong reflector. No discernable drape of post-failure sediment was observed anywhere within this survey.

3.1.5. Scar with headwall in > 715 mwd

Three overlapping AUV surveys covered an ~8 km-long segment of a slide scar in 715 to 990 mwd. This slide scar merges with the other scars below ~1100 mwd to become more than 100 km wide (Fig. 1).

The seafloor upslope of the scar is smooth, undeformed, lacking contour-parallel swales, and dips at ~1° (Fig. 6A, B and C). Here, Chirp profiles show a ~ 70 ms TWT (~53 m) thick unit containing seafloor-parallel, laterally continuous, closely spaced reflections suggesting layered sediments (LS - Fig. 7G).

The scar is composed of a series of arcuate to semicircular escarpments of varying sizes. Within the two largest semicircular scars are staircases of terraces that average 220 m across (T - Figs. 6B and C). The uppermost terraces merge with the surrounding undeformed seafloor, suggesting upper terraces are incompletely severed from the surrounding seafloor (MT - Figs. 6B).

Reflection patterns in Chirp profiles show that the uppermost terraces are rotated blocks of strata which are otherwise indistinguishable from the undeformed layered strata upslope of the slide (RB, LS - Fig. 7G). The thickness of the rotated blocks near the head of the slides is > 40 ms TWT (i.e., ≥ 30 m). Distinctive ridges are observed along the outer edges of the terraces, which are > 400 m long, ≤ 35 m wide, and ≤ 5 high (R - Fig. 6B). The morphology becomes more irregular downslope as individual terraces, ridges, and rotated blocks become less sharply defined (T, R, RB - Fig. 6) and Chirp profiles transition to chaotic reflections with no identifiable internal continuous strata (DW - Fig. 7). This volume of chaotic material forms a wedge situated on top of a sharp boundary below which thinly layered laterally continuous reflectors occur (DW - Fig. 7F and G). This deep layered unit is truncated in a few places along secondary escarpments.

Tongues of jumbled debris composed of individual blocks of talus with up to 5 m of relief and at least 50 m in length cover the bottom of the scar (Fig. 6E). Nowhere within the landslide is there evidence of a post-failure hemipelagic sediment drape thick enough to be detected (> 0.2 m) in the Chirp profiles.

3.1.6. Morphology of the slope away from the scars

The areas outside the scars below ~200 mwd are smooth with average slopes of < 1.3° and consistently underlain by a ≥ 30 m-thick layer of parallel reflections that represents well stratified sediments, which in turn overlies an acoustically homogeneous unit. The surveys in ≤ 350 mwd all show subtle contour-parallel ≤ 1 m-high swales, spaced between 50 and 250 m apart superimposed on an otherwise smooth surface (S - Fig. 3B). The swales are usually bounded by stratal disruptions which occasionally are coincident with small faults of nominal throw. These stratal disruptions (Hill et al., 1982) trace downward to the base of the well layered zone before their continuity is lost within the underlying homogeneous unit (SD - Figs. 7A, B and C). Some of these stratal disruptions trace up to the seafloor while others terminate within the sediment column. Contour-parallel swales are not seen in the two deeper surveys > 500 mwd (Figs. 5 and 6).

3.2. ROV observations

3.2.1. Dives within shelf edge slump with staircase of terraces in > 130 mwd

Five ROV dives took place within this survey area (Fig. 4A and B): three dives on the shelf crossed the PLFs (M16, M25, and M27), one ran up the headwall scarp (M10), and one inspected the ridges associated with the rotated blocks (M26). The three dives on the PLFs revealed that a pebble-rich lag gravel is exposed on their flanks (Fig. 8A). The gravels vary from angular to well-rounded in shape, and are composed of mixed lithologies (Fig. 8B). Clasts were infrequent on the flatter seafloor away

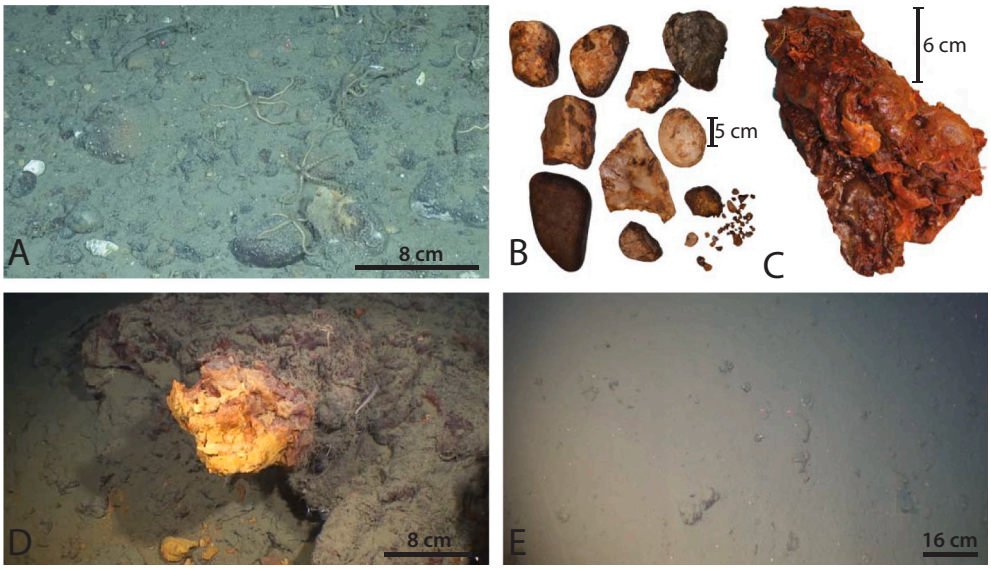

Fig. 8. ROV collected video images and sample photographs showing distinctive features observed during ROV dives within the AUV mapping areas. A - Gravel exposed on top of circular topographic high in 115 mwd during ROV dive M16 within the unfailed section of the *Shelf Edge Scar with Staircase of Terraces in > 130 mwd* AUV survey. B - Gravel clasts of diverse lithologies picked up on that dive. Locations for A and B are denoted with a blue square in Fig. 4A. C- Sample of orange crust from 890 mwd suggesting concentric layers of crust. D- Bright orange sediment crust on side of mound at base of secondary scarp in 890 mwd within the *Scar with Headwall in > 715 mwd* survey. *E*- Matrix-supported cobles exposed on the face of the secondary scarp in 858 mwd within the *Scar with Headwall in > 715 mwd* survey area. Locations for C, D and E are denoted with a blue square in Fig. 6A and D. (For interpretation of the references to colour in this figure legend, the reader is referred to the web version of this article.)

from PLFs. The seafloor surface on dives M10 and M26 was visually unremarkable and devoid of clasts or exposed bedding (Fig. 4).

3.2.2. *Dives within shelf edge scar with adjacent remnant section in > 141 mwd*

During dives M79 and M83, transects were run upslope from the floor of the scar between 253 and 221 mwd and 231–193 mwd (Fig. 4A). The floor of the scar on both sides of the remnant is composed of fine-grained sediment and is visually homogeneous except for two small (< 20 m) patches of blocky cohesive mud rubble. Attempts to push core within the floor of the scar indicated there was only a thin veneer (~10 cm) of soft sediment overlaying firm strata. Nearly horizontal ≤ 5 cm-thick bedding planes exposed between 245 m and 232 mwd on the east side of the remnant appeared to be composed of cohesive clay.

3.2.3. *Dives within scar with headwall in > 519 mwd*

The scar was investigated on dive M15 with a 580 m long transect going upslope between 665 and 597 m water depth to inspect the staircase of terraces along the headwall (Fig. 5A). The seafloor along this transect had a consistently smooth texture and was visually unremarkable and similar to that observed in dives M10 and M26 (Section 3.2.1).

3.2.4. *Dives within scar with headwall in > 715 mwd*

Three short ROV dives (M21, M22, and M80) targeted an area near the base of a secondary escarpment (SE - Fig. 6A and D) in ~890 mwd. These dive were conducted where Chirp profiles show the potential outcropping of the continuous plane that underlies the acoustically chaotic top unit, and of the truncated strata below this unit (FP - Fig. 7F). Mounds covered with bright orange to rust colored surface stains and protruding ~1 m above the surrounding seafloor were encountered (Fig. 8C and D). Another ROV dive (M81) made a transect ~4.5 km farther to the west that extended between 964 and 890 mwd (Figs. 6A and 7G). Similar bright orange stains were encountered on this dive in 901 mwd on a ~ 20° slope, which appeared to be nearly continuous along strike (Fig. 6A). These orange stained deposits appear to be common, approximately ten were encountered on these short ROV dives (Fig. 6A and D). Energy dispersive X-ray spectroscopy with a scanning electron microscopy (EDX-SEM) analysis shows that the bright orange material (Fig. 8C and D) is an iron oxide or iron hydroxide precipitate.

Shimmering water was observed apparently rising out of two of these orange mounds (https://www.mbari.org/arctic-shelf-edge/). A thermal probe inserted ~18 cm into an orange colored mound on dive M80 did not register a significant change (> 0.01 °C) from the ambient temperature. Abundant krill were seen swarming in the immediate vicinity of the orange stained areas, especially after the seafloor was disturbed, but cold seep biological communities, which indicate the presence of seeping sulfide or methane, were not observed (e.g., Paull et al., 2015a).

The steeply sloping sections of the escarpment near the orange stained area (Fig. 6A) observed in ROV dives consisted of cohesive clays with pebbles and cobbles sticking out of the surface (Fig. 8E). Some resistance was encountered when pulling the clasts from the sediment wall, suggesting that the sediments were consolidated.

Two push cores were taken within this escarpment wall (Figs. 6A and D) for ^{210}Pb analysis. One push core (M80 PsC-R2, 14 cm long, 882 mwd) was taken close to an orange mound near the base of the secondary scarp (Figs. 6D and 9A). The other core (M81 PsC-R1, 19 cm long, 964 mwd) was taken on smooth sediment with no significant relief nearby (Figs. 6A and 9B).

4. Discussion

The AUV surveys illustrate the detailed morphology and shallow sub-bottom structure within scars on the slope of the Canadian Beaufort Sea and reveal the stages in the development of a large slope failure. The scars coalesce downslope into a > 100 km wide slope failure complex (Mosher, 2009; Mosher et al., 2012; Saint-Ange et al., 2014; Cameron and King, 2019; Mosher and Hutchinson, 2019).

4.1. *Morphology of the slide scars and failure planes*

The upslope extent of these slide scars is sharply defined by distinct headwall and sidewall scarps with slopes commonly in excess of 20°. These scarps in places expose the truncated edges of the adjacent layered strata (TS - Fig. 7E, F, and G). The bathymetric relief on these scarps is commonly 30–50 m (Figs. 4, 5 and 6) and provides a constraint on the minimum thickness of the section removed by the failures.

Staircases of terraces (T - Figs. 4, 5, and 6) composed of fault-bounded rotated blocks (RB - Fig. 7D, E, F, and G) below the headwall show a distinctive morphology characteristic of retrogressive slides (Gauer et al., 2005; Vanneste et al., 2014; Puzrin et al., 2017). The spacing of these rotated blocks are comparable to the spacing of the slope-parallel swales above or adjacent to the slide scars (Figs. 3 and 4),

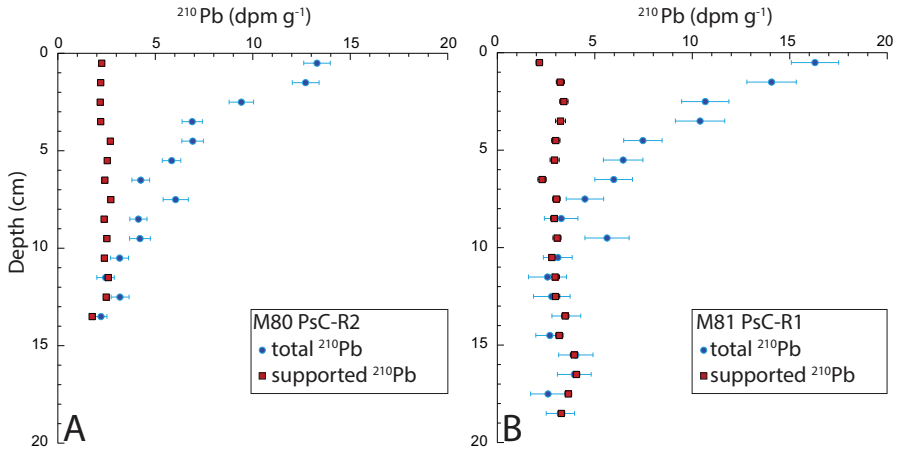

Fig. 9. Downcore profiles of total (blue filled circles) and supported (red squares) ^{210}Pb activity in push cores (A - M80 PsC R2 and B - M81 PsC R1) ± 2SD error bars. Both cores were taken on the surface of the *Scar with Headwall in > 715 mwd* AUV survey at locations shown in Fig. 6. (For interpretation of the references to colour in this figure legend, the reader is referred to the web version of this article.)

suggesting the faults that created the rotated blocks developed along a pre-existing weakness associated with the stratal disruptions (SD - Fig. 7). However, similar swales were not observed in the two deeper surveys. Instead, small faults scarps parallel to the sidewalls suggest that incomplete failures have occured (SS - Fig. 5B) and may further develop in the future.

Near the headwalls, where displacements are modest, the original stratigraphy within the rotated blocks is well preserved even though they have been tilted up to 15° in both upslope and downslope directions (RB - Fig. 7D, E, and G). The base of the layered units within the rotated blocks is typically sharp with an acoustically transparent unit beneath. In places the acoustically transparent unit extends upward along the edge of the rotated blocks (RB - Fig. 7D and E). The uppermost terraces commonly have distinctive < 3 m high, ≤ 30 m wide, > 100 m long ridges on the edges of terraces (R, T - Figs. 4C, 5A, B, 6B, and C). These ridges occur along the bounding faults of the rotated blocks, are elevated above the adjacent terraces, and occur where the stratification at their bases has been lost. These observations suggest that soft sediment was squeezed out from depth along these faults as the blocks rotated to form ridges (R - Figs. 4C, 5B and C, 6B and C).

The ~100 m terrace widths, > 1 km lengths and 10's of m thickness of the rotated blocks show the scale of the individual failure components. Downslope, the blocks become progressively more fragmented, the debris wedge over the failure plane thins-out, and in places almost all the original sediment cover has been evacuated (DW, FP - Figs. 7C - G). This indicates that the excavated sediment mass lost its internal cohesion sufficiently to be transported out of the survey area into the basin below during large upslope propagating retrogressive slope failure events (e.g., Gauer et al., 2005; Vanneste et al., 2014; Puzrin et al., 2017).

The shape of elongated large pieces of debris on the surface of the scars suggests that they are fragments of the distinctive terrace-rimming ridges (Figs. 5C and 6E). These debris wedges are part of the mass transport deposits left after catastrophic failures.

The observed thickness of well layered sediment within the rotated blocks and projections of undeformed sediments under the slide debris help constrain the depth of the initial failure surfaces. A minimum depth for the failure planes of 30 to 50 mbsf is estimated from the thickness of parallel reflections within the rotated blocks (RB, LS, FP - Fig. 7D, E and G). A thickness of ≤ 75 mbsf is inferred from the projection upslope toward the headwalls of undeformed intact horizons visible underneath the debris wedge (HW- Fig. 7D, E, and G). These observations suggest the basal failure surfaces associated within the surveyed slide scars were between 30 and 75 mbsf before the failure event(s). The failure planes are generally parallel with the bedding, but also periodically step up into shallower horizons at secondary scarps within the slide scars (FP - Fig. 7E, F and G), suggesting that the failures were not restricted to one particular weak horizon.

4.2. Timing of slope failures

Radiocarbon measurements on the background unfailed slope sediments are available from JPC 15, a 13.35 m-long piston core taken 687 m water depth in this area (Keigwin et al., 2018; Klotsko et al., 2019; Fig. 1). These measurements show sedimentation rates starting at 10's of cm per thousand years, but increasing with depth to ~6 m per thousand years during deglacial times.

The AUV surveys were all conducted across the uppermost head- (or side) walls of the slide complexes. Due to the retrograde nature of the slumps, areas covered by the surveys are thus associated with the most recent failures. The lack of observable post-failure hemipelagic sediment drapes in the AUV Chirp profiles (Fig. 7) and the rugose surface morphologies inside the slide scars seen in the multibeam data (Figs. 4, 5, and 6) suggest that not enough time has passed to cover the surface of any of the surveyed slides with a sediment layer thick enough to be identified in the Chirp profiles (i.e., > 20 cm).

^{210}Pb profiles from two ROV-collected push cores taken in the soft surficial hemipelagic sediment drape covering the surface of the *Scar with Headwall in > 715 mwd* (Fig. 6) show excess ^{210}Pb activity that decreases gradually down to ~10 cm below seafloor (Fig. 9). These data suggest that sediments accumulated undisturbed on top of this slide surface for more than 136 years, given the 22.6-year half-life of ^{210}Pb and a detection limit of 1%. These measurements are generally consistent with other ^{210}Pb measurements of hemipelagic sediment drape on the Beaufort Slope (Cameron et al., 2017).

Mosher (2009) has suggested that the failure event that produced the 22-km wide scar segment near the shelf edge could have produced a tsunami. While no tsunamis are known to have occurred along the Canadian Beaufort Sea in historic times (<200 years; Leonard et al., 2014), storm surge deposits are common along the Beaufort coast, but are difficult to distinguish from tsunami deposits (Reimnitz and Maurer, 1979; Harper et al., 1985). Earthquake occurrence maps show a distinct cluster of events under the Beaufort Slope and outer shelf in the immediate vicinity of the slide scars (Hyndman et al., 2005; Audet and Ma, 2018). While historical earthquake events recorded in the Canadian Beaufort Sea had magnitudes less than 6.5 (Hyndman et al., 2005), a

recent reassessment of the seismic hazard model used as a basis for the Canadian Building Code has invoked the possibility of a thrust fault beneath the Beaufort Slope with potential for a magnitude 7.8 earthquake (Allen et al., 2015). Earthquakes of this magnitude could provide a trigger for synchronous slope failures along this margin.

4.3. Preconditioning for slope failure?

A remarkably common attribute of all of the slope failures here is that they merge downslope. The systematic multibeam coverage in the area only reaches down to ~1500 mwd. However, by this depth the scar formed by the merging of upslope failures extends laterally along the margin for > 100 km (Saint-Ange et al., 2014; Cameron and King, 2019) and connects with mass transport deposits that extend downslope for > 600 km (Mosher and Hutchinson, 2019). This suggests this area is especially susceptible to large-scale slope failures. Moreover, the similarity of morphology among the slump scars (Figs. 4, 5 and 6) suggests a common failure mechanism.

4.3.1. Rapidly accumulating glacial marine deposits

The consistent depth of the failure planes between 30 and 75 mbsf (FP - Fig. 7C, E, F and G) within the upper reaches of the failures suggests weaknesses in this interval. ROV observations indicate the unit which underlies the failure plane is composed of diamicton facies (Fig. 8A, B, and E) with pebbles and cobbles up to 30 cm in diameter. The varied pebble lithologies in the diamicton imply a glacial origin. Ice shelves extending into the Arctic Ocean from Amundsen Gulf and the Mackenzie Trough ≥ 10,000 years ago have been proposed as the source for glacial deposits (e.g., Margold et al., 2015; Klotsko et al., 2019). However, the deeper reaches of these slide scars cut into much older stratigraphy suggesting that the failures are not restricted to a particular horizon (Fig. 7G).

Sedimentation rates in the study area (Fig. 1) during the late Holocene (Keigwin et al., 2018; Klotsko et al., 2019) are only 10's of cm per thousand years. This suggest that this area is not receiving large inputs of sediment from the Mackenzie River (Rachold et al., 2000; Holmes et al., 2002). In contrast, the ~6 m/1000 yr sedimentation rate during deglacial times (Keigwin et al., 2018; Klotsko et al., 2019) is anomalously rapid compared to most continental slope settings, but not unknown in other glaciomarine settings (Sommerfield, 2006). Moreover, still higher sedimentation rates may have occurred during glacial times.

Clay present in the matrix of glaciomarine diamicton reduces permeability and impedes compaction and dewatering. Thus, such rapidly accumulating glaciomarine sections are prone to experience elevated pore pressure, a factor that can weaken the sediments and cause slope instability (e.g., Pope et al., 2018).

Similar Arctic settings off Norway, which also experienced high sedimentation rates, contain many of the world's largest slides scars (Bugge et al., 1988; Solheim et al., 2005; Laberg and Vorren, 2000; Lindberg et al., 2004). Rapid glaciomarine sedimentation has been considered a partial contributing factor to these slides. By analogy, high sedimentation rates are also likely a pre-conditioning factor for the failures on the Beaufort Slope. While the period of high sedimentation rates ended more than 10,000 years ago (Keigwin et al., 2018; Klotsko et al., 2019), the pre-condition and propensity for failure of slope sediments persist. Thus, additional pre-conditioning factors should also be considered.

4.3.2. Slope steepness

The areas adjacent to the mapped slides on the Beaufort Slope consistently have slopes of < 1.7°, which is not uncommonly steep on depositional slopes (Booth et al. Środoń, 1999; Masson et al., 2010). The majority of the > 100 km wide coalesced failure scars below ~1100 mwd developed in areas with similar average slope angles. Moreover, some areas on the Beaufort Slope are steeper (i.e., ≤ 3.6°) and have not failed. Thus, high pre-failure depositional slope angles do not appear to be a primary pre-conditioning factor.

4.3.3. Implications of Arctic cold-water lid

An unusual aspect of the Canadian Beaufort Sea is the shallow cold-water layer with mean annual temperatures of ≤ −1.5 °C that impinges on the shelf edge seafloor down to ~200 mwd (McLaughlin et al., 2004; Melling, 1998). Brackish waters freeze at these temperatures (Millero and Leung, 1976). Freezing of the brackish waters that infuse the shelf edge and upper slope strata in this area (Gwiazda et al., 2018) might deform near seafloor sediment and stimulate slope failures. Seafloor deformation associated with intra-sediment freezing along the Beaufort Shelf edge is indicated by the presence of a band of numerous PLFs (Saint-Ange et al., 2014; Paull et al., 2019; Figs. 1 and 4). However, the majority of the failures along the Beaufort Slope are in > 1 km water depth, well below where freezing of brackish water is possible. Only in one place (*Shelf Edge Scar with Adjacent Remnant Section in > 141 mwd*) does the headwall of the slide connect with potentially permafrost-bearing shelf edge strata, and this coincidence may be the result of upslope slide retrogression. Thus, proximity to the shelf edge and the resulting bathing of sediments ≤ 200 mwd by subzero degree waters do not appear to play a major role in stimulating the observed widespread failures.

4.3.4. Interstitial gas and gas hydrate

Because the occurrence of interstitial gas bubbles reduces sediment shear strength and the decomposition of gas hydrate can also lead to the formation of gas overpressure, they have long been suspected to play a role in submarine slope failures worldwide (e.g., Hampton et al., 1978; Paull et al., 2000). Gas hydrate decomposition has been postulated as a possible cause of slope instability in the Beaufort Sea (e.g., Saint-Ange et al., 2014; Nixon and Grozic, 2007). Indeed, methane bubbles have been observed escaping from the seafloor from the top of mid-shelf PLFs (Paull et al., 2007), along the edge of the Beaufort Shelf (Paull et al., 2011), and from mud volcanoes on the slope (Blasco et al., 2013; Saint-Ange et al., 2014; Paull et al., 2015a). Samples of gas hydrate have been taken from a seep site on the Alaskan Beaufort Slope (Edwards et al., 2011; Pohlman et al., 2011). However, the existence of isolated seeps does not necessarily imply that free gas or gas hydrates are widely distributed within the slope sediments.

Three observations suggest that interstitial methane bubbles are not widespread within the slope sediments at the depths of the observed failure planes. (1) Bottom simulating reflectors, a common indicator of the presence of free gas near the base of a gas hydrate bearing zone, are notably absent in seismic reflection profiles from the relevant areas on the Canadian Beaufort Slope (Riedel et al., 2017; Fig. 2). While some multichannel seismic lines show enhanced amplitudes at depth, which are possibly indicative of free gas within Pliocence strata, they are well below the observed slope failure planes (amplitude anomalies - Fig. 2) and there are no seismic indications (Løseth et al., 2009) that free gas is leaking up to the seafloor under the slope in the vicinity of the failures. (2) High resolution AUV Chirp profiles and multichannel seismic lines of slope sediments, where the upslope propagating retrogressive slides initiated, lack distinctive acoustic blanking patterns indicative of the presence of free gas (Judd and Hovland, 1992; Fig. 2). The sub-bottom resolution is unusually deep and laterally consistent compared to other regions using the same Chirp system (Paull et al., 2015a, 2015b). Moreover, pore waters in sediment cores taken from the shelf edge where patches of acoustic blanking do occur (Fig. 7 B and C) have steep chloride but gentle sulfate pore water concentration gradients (Fig. 10A and C) suggesting the blanking results from permafrost cementation instead of the presence of gaseous methane (Borowski et al., 1996). (3) In the slide scars where iron oxide or hydroxide mounds and shimmering water were observed (Fig. 8C and D), no evidence, such as chemosynthetic seep fauna or methane-derived authigenic carbonate (e.g., Paull et al., 1992; Kiel, 2010), was seen that would indicate significant concentrations of methane are carried in the venting water.

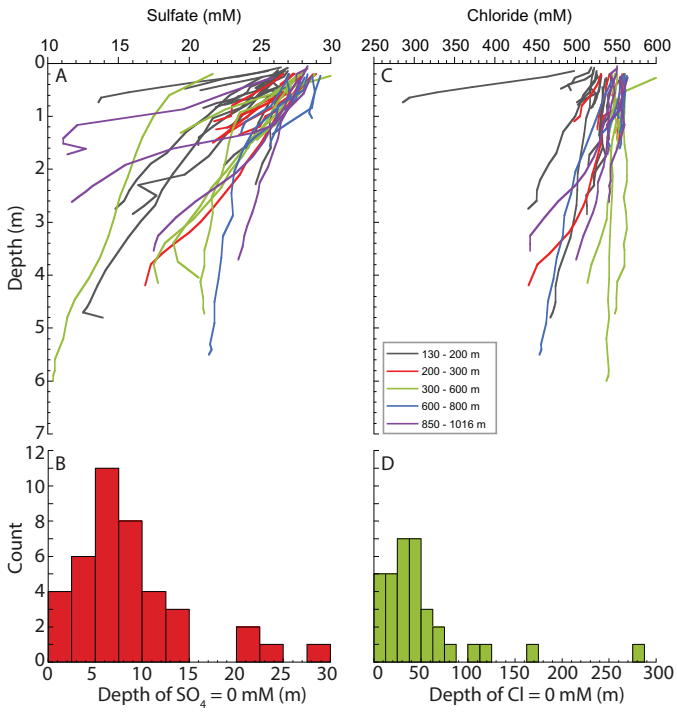

Fig. 10. Concentrations of pore water sulfate (A) and chloride (C) versus sub-bottom depth of Beaufort Sea cores from water depths between 130 and 1016 m with statistically significant linear gradients (p values <0.05). Also shown are histograms of the depths in meters at which the sulfate (B) and chloride (D) extrapolated gradients would indicate a zero concentration.

For gas hydrate decomposition to stimulate widespread, late Holocene failures, a change in physical conditions (i.e., chemical composition, pressure, or temperature) would be required. Usually, the salinity of pore water within the first few hundreds of meters below the seafloor remains similar to seawater. The freshening in the pore water salinity observed in the sediment cores (Fig. 10C) is uncommon (Borowski et al., 1999). The elemental and isotopic composition of the freshening water is inconsistent with a gas hydrate decomposition origin (Pohlman et al., 2011; Gwiazda et al., 2018). Furthermore, the decrease in salinity associated with the infusion of brackish water acts to expand the gas hydrate stability field (Dickens and Quinby-Hunt, 1997) which by itself would likely act to increase rather than decrease slope stability (Winters et al., 2007).

For a seafloor pressure decrease to stimulate gas hydrate decomposition, uplift associated with glacial rebound would have had to occur at a rate that exceeded eustatic sea level rise (Dyke and Peltier, 2000). Post glacial isostatic adjustment on the Beaufort Shelf was limited as this area was not extensively ice covered during the last glaciation (Rampton, 1988; Dyke, 2004; England et al., 2009) and the relative sea level data from the Beaufort Sea indicates that the shelf area has been subsiding throughout the late Holocene (Hill et al., 1985). Thus, the observations suggest that in the Holocene a net seafloor pressure increase has occurred which would act to stabilize gas hydrate in the slope, not stimulate its decomposition.

The existence of temperature variations associated with the deep-waters within the Arctic Ocean throughout the Holocene are largely unknown. The marine gas hydrate stability field forms a wedge where the up-dip limit of the marine gas hydrate stability zone in sediments thins before vanishing. The volume expansion associated with gas hydrate decomposition increases at shallower water depths, leaving the sediments within the up-dip limit of the gas hydrate stability zone increasingly susceptible to failure associated with either temperature or pressure changes (Booth et al., 1994; Paull et al., 2000; Westbrook et al., 2009; Ruppel, 2011). In the Canadian Beaufort Sea, the depth where the up-dip limit of the gas hydrate stability zone in sediments thins and vanishes is presently at ~282 mwd (e.g., Paull et al., 2015a). The observed slope failures on the Beaufort Slope are not preferentially concentrated nor start in a band near this depth (Figs. 1 and 3). Taken together, the available observations do not indicate the slope in the Canadian Beaufort Sea is especially susceptible to failures associated with the widespread occurrence of interstitial free gas or gas hydrate decomposition.

4.3.5. *Widespread infusion of brackish waters within slope sediments*

Previously published pore water chloride concentration gradients of cores from the Beaufort Shelf edge and Slope (Fig. 10C) show a systematic freshening with depth (Paull et al., 2011, 2015a; Gwiazda et al., 2018). Data from these studies supplemented with additional cores from 130 to 1016 mwd (see Supplementary Table 1) show 34 statistically significant (i.e., $p < 0.05$) chloride gradients. Extrapolations of the existing pore water gradients (Fig. 10C; Paull et al., 2011, 2015a; Gwiazda et al., 2018) suggest that fresh water occurs at a median depth of 38 mbsf within the study area (Fig. 10D). Irrespective of whether truly fresh water is the appropriate end member, the gradient extrapolations indicate that waters at the depth of the failure plane (30–75 mbsf) are considerably fresher than seawater. The existence of brackish waters within slope sediments along continental margins is uncommon (Borowski et al. Środoń, 1999) and its impact on slope stability should be considered.

The sedimentary section underlying the Beaufort Slope where slope failures are found was deposited within a marine environment presumably trapping seawater at deposition along with clay minerals during latest Pleistocene and early Holocene times (Keigwin et al., 2018; Klotsko et al., 2019). The presence of fresher waters now within the slope sediment has been attributed to infusion with water from decomposing relict permafrost near the shelf edge and regional ground water flow underneath the relict permafrost at greater depths (Gwiazda et al., 2018; Fig. 11).

The effect of the observed pore water salinity change on the clay mineral properties in the slope sediments should be considered. The

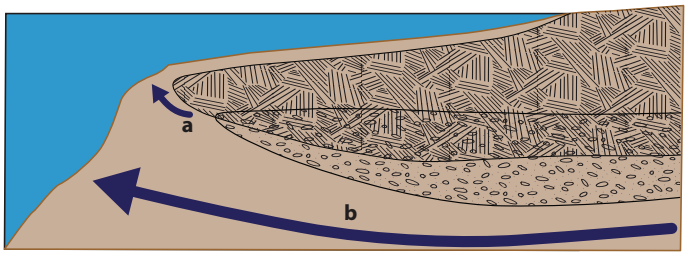

Fig. 11. Schematic representation of flow paths for the brackish waters infusing into shelf edge and slope sediments of the Canadian Beaufort Sea after Gwiazda et al. (2018). They infer in the shelf edge the brackish waters are derived from permafrost decomposition at the base of the permafrost (a) and in the slope from regional groundwater flow underneath the permafrost (b). Hatched and stippled patterns represent permafrost and gas hydrate zones, respectively.

hydro-mechanical behavior of most clay particles is affected by changes in salinity (e.g., Rolfe and Aylmore, 1977; Locat and Demers, 1988; Di Malo, 1996; Barbour and Yang, 1993; Laird et al., 1995; Deng et al., 2011; Nguyen et al., 2013; Zhang et al., 2019). Increases in salinity result in changes in the bonding strength between grains in most types of clays and a susceptibility to swelling in some clays. For marine sediments changes in the bonding strength start with clay flocculation when suspended clay traveling in fluvial transport systems first encounter the higher salinities of seawater (Al Ani et al., 1991; Sutherland et al., 2015). After deposition, the effective stress continues to change with the salinity (Torrence, 1983; Bjerrum, 1954). However, the changes are reversible (Laird et al., 1995; Di Malo, 1996; Morsy and Sheng, 2014). A decrease in pore water salinity will result in a decrease in clay bonding. Thus, clay rich strata originally deposited in open marine sediments that have been flushed with fresher water after deposition may be preconditioned for failure.

Samples of the sediment at the depth of the inferred failure plane for the surveyed failures are not available. The existing knowledge of the clay mineral composition of the sediments rimming the Arctic suggests illite (a non-expanding clay) is the dominant clay (Kalinenko, 2001). Nevertheless, the permeability of even illite-dominated cores does change markedly with electrolyte concentrations (i.e., salinity; Rolfe and Aylmore, 1977). However, swelling clays are a common secondary component of Arctic clays (Kalinenko, 2001). The sediments found at depth under the Beaufort-Mackenzie Basin are dominated by illite/smectite mixed-layered clays with smectite predominating at shallower depths (Ko and Hess, 1998; Ko and Hesse, 1995). Smectite in mixed-layered clays are subject to swelling with increased salinity (Goldberg et al., 1991; Środoń, 1999). When appropriate samples of clay minerals along the failure plane become available, their role as a preconditioning agent for failure could be weighed further.

4.3.6. *Brackish water springs within slide scars*

The fortuitous discovery of the orange stained mounds and shimmering water (https://www.mbari.org/arctic-shelf-edge/) indicates that there is advective water flow coming out onto the seafloor from strata associated with the exposed, acoustically homogeneous unit. The shimmering visual effect is produced by mixing of waters with different refractive indices, usually related to temperature or salinity differences. The lack of a temperature anomaly in the thermal probe measurements indicates that the rise of the shimmering waters was not driven by heat, and that the shimmering effect is due to salinity differences between seawater and the emerging fluid. The lack of chemosynthetic biological communities known to colonize methane seeps, suggests the springs associated with the orange iron precipitate are not carrying significant concentrations of methane (Kiel, 2010). Iron precipitates like those observed on the mounds are characteristic of brackish or fresh water springs which carry reduced iron to the seafloor where it precipitates when oxygenated seawater is encountered (Charette and Sholkovitz, 2002). The discovery of 10 similarly appearing orange mounds during just three short ROV dives covering ~200 m long transects and another one 4.5 km away suggests that submarine springs are common within these slide scars (Fig. 6A & D and 8C & D). The existence of seafloor springs carrying brackish waters to the seafloor requires a pressure gradient to drive the flow, which is another indication of overpressured conditions. However, the Arctic margin has not been adequately sampled to assess how widespread the presence of brackish pore waters is within the Arctic Slope.

5. Conclusions

Detailed surveys along the upper continental slope of the Canadian Beaufort Sea provide documentation of the scars left by large retrogressive submarine landslides, and of the character of non-failed, near-seafloor sediments in adjacent areas. The slides have failure planes that were initially between 30 and 75 mbsf within glacial marine deposits. The morphology indicates major failures occurred as discrete large-scale events which retrogressed upslope. The overlying material initially broke up into rotated blocks which preserved the original stratigraphy, but with increasing downslope transport, blocks disaggregated and the materials flowed out of the survey areas. Minimal drape of hemipelagic sediment has accumulated since the failure(s) occurred, indicating that these scars are geologically recent.

Attributing a particular failure mechanism to any slide scar is inherently difficult. Rapid sedimentation during last glacial periods is likely a factor in preconditioning the Beaufort Slope for failure. The role of free gas and gas hydrate could be invoked, but it is not clear that the sediments on the Beaufort Slope near the failure plane are especially gas or hydrate charged. A rather unique characteristic of the Beaufort Slope is widespread occurrence of brackish waters at the depth of the failure plane. As these sediments were deposited under marine conditions, pore water freshening would imply sediments have been flushed with brackish waters. Flushing is also consistent with the spring flow observed emanating from the slide scars walls, which in turn indicates overpressured conditions. Overpressure and a reduction in pore water salinity may both act to reduce the mechanical strength of clays and precondition these sediments for failure.

Data availability

Bathymetric datasets are available from the Marine Geoscience Data System repository at: https://www.marine-geo.org/tools/search/entry.php?id=Arctic_MBARI

Declaration of Competing Interest

The authors declare that they have no known competing financial interests or personal relationships that could have appeared to influence the work reported in this paper.

Acknowledgements

Support was provided by the David and Lucile Packard Foundation; the Canadian Program of Energy Research and Development (PERD) to

both the Geological Survey of Canada, and Fisheries and Oceanography Canada; and by the Ministry of Ocean and Fisheries, Korea to the Korea Polar Research Institute (KIMST No. 20160247). The success of these cruises is attributed to the professionalism of the officers and crews of CCGS *Sir Wilfrid Laurier* and *Araon*. The regional multibeam coverage is provided though ArcticNet, a joint academic/industry research consortium. We also appreciate the insightful reviews by Jason Chaytor and two annomous reviewers. Any use of trade, firm, or product names is for descriptive purposes only and does not imply endorsement by the U.S. Government.

Appendix A. Supplementary data

Supplementary data to this article can be found online at https://doi.org/10.1016/j.margeo.2021.106453.

References

Al Ani, S., Dyer, K.R., Huntley, D.A., 1991. Measurement of the influence of salinity on floc density and strength. Geo-Marine Letters 11, 154–158. https://doi.org/10.1007/BF02431002 Download citation.

Allen, T.I., Adams, J., Halchuck, S., Rogers, G.C., 2015. 5th Generation seismic hazard model for northwestern Canada. In: Proceedings 11th Canadian Conference on Earthquake Engineering, Paper 93782, 13 p.

Audet, P., Ma, S., 2018. Deep crustal earthquakes in the Beaufort Sea, Western Canadian Arctic, from Teleseismic depth phase analysis, 2015. Seismol. Res. Lett. 89 https://doi.org/10.1785/0220180047.

Barbour, S.L., Yang, N.A., 1993. Review of the influence of clay-brine interactions on the geotechnical properties of Ca-montmorillonitic clayey soils from western Canada. Can. Geotech. J. 30, 920–934.

Batchelor, C.L., Dowdeswell, J.A., Pietras, J.T., 2013. Variable history of Quaternary ice-sheet advance across the Beaufort Sea margin, Arctic Ocean. Geology 41, 131–134. https://doi.org/10.1130/G33669.1.

Bjerrum, L., 1954. Geotechnical properties of Norwegian marine clays. Geotechnique 4, 49–69.

Blasco, S.M., Fortin, G., Hill, P.R., O'Connor, M.J., Brigham-Grette, J.K., 1990. The Late Neogene and Quaternary stratigraphy of the Canadian Beaufort Continental Shelf. In: Grantz, A., Johnson, L., Sweeney, J.F. (Eds.), The Arctic Ocean Region, Boulder, Colorado, Geological Society of America, The Geology of North America series, Vol. L, pp. 491–502. Chapter 28.

Blasco, S., Bennett, R., Brent, T., Burton, M., Campbell, P., Carr, E., Covill, R., Dallimore, S., Davies, E., Hughes-Clarke, J., Issler, D., MacKillop, K., Mazzotti, S., Patton, E., Shearer, J., White, M., 2013. 2010 state of knowledge: Beaufort Sea seabed geohazards associated with offshore hydrocarbon development. In: Geological Survey of Canada Open File 6989. https://doi.org/10.4095/292616, 307 pp.

Booth, J.S., Winters, W.J., Dillon, W.P., 1994. Circumstantial evidence of gas hydrate and slope failure associations on the United States Atlantic continental margin, Natural Gas Hydrates. Ann. NY Acad. Sci. 715, 487–489.

Borowski, W.S., Paull, C.K., Ussler III, W., 1996. Marine pore water sulfate profiles indicate methane flux from underlying gas hydrates. Geology 24, 655–658.

Borowski, W.S., Paull, C.K., Ussler III, W., 1999. Global and local variations of interstitial sulfate gradients in deep-water, continental margin sediments: sensitivity to underlying gas hydrates. Mar. Geol. 159, 131–154.

Bugge, T., Belderson, R.H., Kenyon, N.H., 1988. The Storegga slide. Phil. Trans. R. Soc. A 325, 357–388.

Cameron, G.D.M., King, E.L., 2019. Mass-failure complexes on the Central Beaufort Slope, offshore Northwest Territories. In: Geological Survey of Canada Open File 8356, 39 p.

Cameron, G.D.M., King, E.L., Murray, D., Kuzyk, Z.A., Blasco, S., 2017. Relative timing of sediment failures within slide-valley complexes in the Kugmallit Fan area of the Central Beaufort Slope, offshore Northwest Territories. In: Geological Survey of Canada, Scientific Presentation 74, Poster. https://doi.org/10.4095/306013.

Caress, D.W., Chayes, D.N., 1996. Improved processing of Hydrosweep DS Multibeam Data on the R/V Maurice Ewing. Mar. Geophys. Res. 18, 631–650.

Caress, D.W., Thomas, H., Kirkwood, W.J., McEwen, R., Henthorn, R., Clague, D.A., Paull, C.K., Paduan, J., Maier, K.L., 2008. High-resolution multibeam, sidescan, and subbottom surveys using the MBARI AUV D. Allan B. In: Reynolds, J.R., Greene, H.G. (Eds.), Marine Habitat Mapping Technology for Alaska: Alaska Sea Grant College Program. University of Alaska Fairbanks. https://doi.org/10.4027/mhmta.2008.04.

Charette, M.A., Sholkovitz, E.R., 2002. Oxidative precipitation of groundwater-derived ferrous iron in the subterranean estuary of a coastal bay. Geophys. Res. Lett. 29, p. 85-1–85-4.

Deng, Y.F., Cui, Y.J., Tang, A.M., Nguyen, X.P., Li, X.L., Van Geet, M., 2011. Investigating the pore-water chemistry effects on the volume change behaviour of Boom clay. Phys. Chem. Earth 36, 1905–1912.

Di Malo, C., 1996. Exposure of bentonite to salt solutions: osmotic and mechanical effects. Géotechnique 46, 695–707.

Dickens, G.R., Quinby-Hunt, M.S., 1997. Methane hydrate stability in pore water: a simple theoretical approach for geophysical applications. J. Geophys. Res. 102, 773–783.

Dietrich, J.R., Dixon, J., McNeil, D.H., 1985. Sequence analysis and nomenclature of Upper Cretaceous to Holocene strata in the Beaufort-Mackenzie Basin. In: Current Research, Geological Survey of Canada, Paper 85-1A, pp. 613–628.

Dixon, J., Lane, L.S., Dietrich, J.R., McNeil, D.H., Chen, Z., 2019. Geological history of the Late Cretaceous to Cenozoic Beaufort-Mackenzie Basin, Arctic Canada. In: The Sedimentary Basins of United States and Canada. Elsevier, pp. 695–717. Chapter 17.

Dugan, B., Flemings, P.B., 2000. Overpressure and fluid flow in the New Jersey continental slope: implications for slope failure and cold seeps. Science 289, 288–291.

Dyke, A.S., 2004. An outline of North American deglaciation with emphasis on central and northern Canada. In: Ehlers, J., Gibbard, P.L. (Eds.), Developments in Quaternary Sciences. Elsevier, pp. 373–424.

Dyke, A.S., Peltier, W.R., 2000. Forms, response times and variablitity of relative sea-level curves in glaciated North America. Geomorphology 32, 315–333.

Edwards, B.E., Saint-Ange, F., Pohlman, J., Higgins, J., Mosher, D.C., Lorenson, T., Hart, P., 2011. American Geophysical Union Fall Meeting, Abstract PP33A-1915.

England, J.H., Furze, M.F.A., Doupe, J.P., 2009. Revision of the NW Laurentide Ice Sheet: implications for paleoclimate, the northeast extremity of Beringia, and Arctic Ocean sedimentation. Quat. Sci. Rev. 28, 1573–1596.

Frederick, J.M., Buffett, B.A., 2015. Effects of submarine groundwater discharge on the present-day extent of relict submarine permafrost and gas hydrate stability on the Beaufort Sea continental shelf. J. Geophys. Res. 120, 417–432. https://doi.org/10.1002/2014JF003349.

Gauer, P., Kvalstad, T.J., Forsberg, C.F., Bryn, P., Berg, K., 2005. The last phase of the Storegga Slide: simulation of retrogressive slide dynamics and comparison with slide-scar morphology. Mar. Pet. Geol. 22, 171–178. https://doi.org/10.1016/j.marpetgeo.2004.10.004.

Goldberg, S., Forster, H.S., Heick, E.L., 1991. Flocculation of illite/kaolinite and illite/montmorillonite mixtures as affected by sodium adsorption ratios and pH. Clay Clay Miner. 39, 375–380.

Gwiazda, R., Paull, C.K., Dallimore, S.R., Melling, H., Jin, Y.K., Hong, J.K., Riedel, M., Lundsten, E., Anderson, K., Conway, K., 2018. Freshwater seepage into sediments of the shelf, shelf edge and continental slope of the Canadian Beaufort Sea. Geol. Geochem. Geophys. Geosyst. 19 https://doi.org/10.1029/2018GC007623.

Hampton, M.A., Bouma, A.H., Carlson, P.R., Molnia, B.F., Clukey, E.C., Sangrey, D.A., 1978. Quantitative Study of Slope Instability in the Gulf of Alaska. Offshore Technol. Conf. https://doi.org/10.4043/3314-MS.

Hampton, M.A., Lee, H.J., Locat, J., 1996. Submarine landslides. Rev. Geophys. 34, 33–59.

Harper, J.R., Henry, R.F., Stewart, G.G., 1985. Maximum storm surge elevations in the Tuktoyaktuk Region of the Canadian Beaufort Sea. Arctic 41, 48–52.

Hill, P.R., Moran, K.M., Blasco, S.M., 1982. Creep deformation of slope sediments in the Canadian Beaufort Sea. Geo-Mar. Lett. 2, 163–170.

Hill, P.R., Mudie, P.J., Moran, K., Blasco, S.M., 1985. A sea-level curve for the Canadian Beaufort Sea. Can. J. Earth Sci. 22, 1383–1393.

Holmes, R.M., McClelland, J.W., Peterson, B.J., Shiklomanov, A., Shiklomanov, A.I., Zhulidov, V., Gordeev, V.V., Bobrovitskaya, N.N., 2002. A circumpolar perspective on fluvial sediment flux to the Arctic Ocean. Glob. Biogeochem. Cycles 16 (4), 1098. https://doi.org/10.1029/2001GB001849.

Hu, K., Issler, D.R., Chen, Z., Brent, T.A., 2013. Permafrost investigation by well logs, and seismic velocity and repeated shallow temperature surveys, Beaufort-Mackenzie Basin. In: Geological Survey of Canada, Open File 6956. https://doi.org/10.4095/293120, 33 p.

Hu, K., Dietrich, J.R., Chen, Z., Hannigan, P.K., 2018. Petrophysical analyses of hydrocarbon reservoirs and overpressure zones in Tertiary deep-marine strata in the northern Beaufort-Mackenzie Basin, Arctic Canada. In: Geological Survey of Canada, Open File 8368. https://doi.org/10.4095/306960, 36 p.

Huhnerbach, V., Masson, D.G., 2004. Landslides in the North Atlantic and its adjacent seas: an analysis of their morphology, setting and behavior. Mar. Geol. 213, 343–362.

Hyndman, R.D., Cassidy, J.F., Adams, J., Rogers, G.C., Mazzotti, S., 2005. Earthquakes and seismic hazard in the Yukon-Beaufort-Mackenzie. CSEG Recorder 30 (5), 32–66.

Jakobsson, M., Andreassen, K., Bjarnadóttir, L.R., Dove, D., Dowdeswell, J.A., England, J.H., Funder, S., Hogan, K., Ingólfsson, Ó., Jennings, A., Larsen, N.K., Kirchner, N., Landvik, J.Y., Mayer, L., Mikkelsen, N., Möller, P., Niessen, F., Nilsson, J., O'Regan, M., Polyak, L., Nørgaard-Pedersen, N., Stein, R., 2014. Arctic Ocean glacial history. Quat. Sci. Rev. 92, 40–67.

Jin, Y.K., Dallimore, S.R., 2016. ARA05C marine research expedition, Canada-Korea-USA Beaufort Sea Geoscience Research Program: Summary of 2014 Activities. In: Geological Survey of Canada, Open File 7999. https://doi.org/10.4095/297866, 107 pp.

Jin, Y.K., Riedel, M., Hong, J.K., Nam, S.I., Jung, J.Y., Ha, S.Y., et al., 2015. Overview of field operations during a 2013 research expedition to the southern Beaufort Sea on the *RV Araon*. In: Geological Survey of Canada, Open File 7754. https://doi.org/10.4095/295856, 181 pp.

Judd, A.G., Hovland, M., 1992. The evidence of shallow gas in marine sediments. Cont. Shelf Res. 12, 1081–1095. https://doi.org/10.1016/0278-4343(92)90070-Z.

Kalinenko, V.V., 2001. Clay minerals in sediments of the Arctic Seas. Lithol. Miner. Resour. 36, 362–372.

Keigwin, L.D., Klotsko, S., Zhao, N., Reilly, B., Giosan, L., Driscoll, N.W., 2018. Deglacial floods in the Beaufort Sea preceded Younger Dryas cooling. Nat. Geosci. 11, 599–604.

Kiel, S., 2010. The Vent and Seep Biota. Springer, Dordrecht. https://doi.org/10.1007/978-90-481-9572-5.

Klotsko, S., Driscoll, N., Keigwin, L., 2019. Multiple meltwater discharge and ice rafting events in the deglacial sediments along the Beaufort Margin, Arctic Ocean. Quat. Sci. Rev. 203, 185–208.
Ko, J., Hess, R., 1998. Illite/Smectite Diagenesis in the Beaufort-Mackenzie Basin, Arctic Canada: Relation to Hydrocarbon Occurrence? Bulletin of Canadian Petroleum Geology 46 (1), 74–88. https://doi.org/10.35767/gscpgbull.46.1.074.
Ko, J., Hesse, R., 1995. Mineralogy of illite/smectite mixed-layer clays from the Beaufort-Mackenzie Basin, Arctic Canada. Economic and Environmental Geology 28 (4), 327–335.
Laberg, J.S., Vorren, T.O., 2000. The Traenadjupet slide, offshore Norway – morphology, evacuation and triggering mechanisms. Mar. Geol. 171, 95–114.
Laird, D.A., Shang, C., Thompson, M.L., 1995. Hysteresis in crystalline swelling of smectites. J. Colloid Interface Sci. 171, 240–245.
Leonard, L.J., Rogers, G.C., Mazzotti, S., 2014. Tsunami hazard assessment of Canada. Nat. Hazards 70, 237–274. https://doi.org/10.1007/s11069-013-0809-5.
Lindberg, B., Laberg, J.S., Vorren, T.O., 2004. The Nyk slide—morphology, progression, and age of a partly buried submarine slide offshore northern Norway. Mar. Geol. 213, 277–289.
Locat, J., 2001. Instabilities along ocean margins: a geomorphological and geotechnical perspective. Mar. Pet. Geol. 18, 503–512.
Locat, J., Demers, D., 1988. Viscosity, yield stress, remolded strength and liquidity index relationships for sensitive clays. Can. Geotech. J. 25, 799–806.
Locat, J., Lee, H.J., 2002. Submarine landslides: advances and challenges. Can. Geotech. J. 39, 193–212.
Locat, J., Leroueil, S., Locat, A., Lee, H., 2014. Weak layers: their definition and classification from a geotechnical perspective. In: Krastel, S., et al. (Eds.), Submarine Mass Movements and Their Consequences, Advances in Natural and Technological Hazards Research, Vol.. 37. Springer, Dordrecht, Netherlands, pp. 3–12.
Løseth, H., Gading, M., Wensaas, L., 2009. Hydrocarbon leakage interpreted on seismic data. Mar. Pet. Geol. 26, 1304–1319. https://doi.org/10.1016/j.marpetgeo.2008.09.008.
Mackay, J.R., 1998. Pingo growth and collapse, Tuktoyaktuk Peninsula area, western Arctic cost, Canada: a long-term field study. Géog. Phys. Quatern. 52, 271–323.
Margold, M., Stokes, C.R., Clark, C.D., 2015. Ice streams in the Laurentide Ice Sheet: identification, characteristics and comparison to modern ice sheets. Earth Sci. Rev. 143, 117–146. https://doi.org/10.1016/j.earscirev.2015.01.011.
Masson, D.G., Harbitz, C.B., Wynn, R.B., Pedersen, G., Løvholt, F., 2006. Submarine landslides: processes, triggers and hazard prediction. Philos. Trans. R. Soc. Lond. 364, 2009–2039.
Masson, D.G., Wynn, R.B., Talling, P.J., 2010. Large landslides on passive continental margins: processes, hypotheses and outstanding questions. In: Mosher, D.C., Shipp, C., Moscardelli, L., Chaytor, J., Baxter, C., Lee, H., Urgeles, R. (Eds.), Submarine Mass Movements and Their Consequences IV, Advances in Natural and Technological Hazards Series 28. Springer, pp. 153–165.
McLaughlin, F.A., Carmack, E.C., Macdonald, R.W., Melling, H., Swift, J.H., Wheeler, P.A., Sherr, B.F., Sherr, E.B., 2004. The joint roles of Pacific and Atlantic-origin waters in the Canada Basin, 1997-1998. Deep-Sea Res. 51, 107–128.
Melling, H., 1998. Hydrographic changes in the Canada Basin of the Arctic Ocean, 1979–1996. J. Geophys. Res. 103 (C4), 7637–7645. https://doi.org/10.1029/97JC03723.
Millero, F.J., Leung, W.H., 1976. The thermodynamics of seawater at one atmosphere. Am. J. Sci. 276, 1035–1077.
Morsy, S., Sheng, J.J., 2014. Effect of water salinity on shale reservoir productivity. Adv. Pet. Explor. Dev. 8, 9–14. https://doi.org/10.3968/5604.
Mosher, D.C., 2009. International year of Planet Earth 7. Oceans: submarine landslides and consequent tsunamis in Canada. Geosci. Can. 36, 179–190.
Mosher, D.C., Hutchinson, D.R., 2019. Canada Basin: Chapter 10. In: Piskarev, A., Poselov, V., Kaminsky, V. (Eds.), Geologic Structures of the Arctic Basin. Springer, pp. 295–325. https://doi.org/10.1007/978-3-319-77742-9_10.
Mosher, D.C., Shimeld, J.W., Hutchinson, D., Lebedeva-Ivanova, N., Chapman, C.B., 2012. Submarine landslides in Arctic sedimentation: Canada Basin. In: Yamada, Y., Kawamura, K., Ikehara, K., Ogawa, Y., Urgeles, R., Mosher, D., Chaytor, J., Strasser, M. (Eds.), Submarine Mass Movements and Their Consequences V, Advances in Natural and Technological Hazards Research, Vol. 31, pp. 147–158.
Nguyen, X.P., Cui, Y.J., Tang, A.M., Deng, Y.F., Li, X.L., Wouters, L., 2013. Effects of pore water chemical composition on the hydro-mechanical behavior of natural stiff clays. Eng. Geol. 166, 52–64.
Nixon, M.F., Grozic, J.L.H., 2007. Submarine slope failure due to gas hydrate dissociation: a preliminary quantification. Can. Geotech. J. 44, 314–325. https://doi.org/10.1139/t06-121.
Osadetz, K.G., Chen, Z., 2010. A re-evaluation of Beaufort Sea-Mackenzie Delta basin gas hydrate resource potential: petroleum system approaches to non-conventional gas resource appraisal and geologically-sources methane flux. Bull. Can. Petrol. Geol. 58, 56–71. https://doi.org/10.2113/gscpgbull.58.1.56.
Paull, C.K., Chanton, J., Neumann, A.C., Coston, J.A., Martens, C.S., Showers, W., 1992. Indicators of methane-derived carbonates and chemosynthetic organic carbon deposits. In: Examples from the Florida Escarpment, Palaios, Vol. 7, pp. 361–375.
Paull, C.K., Dillon, W.P., Ussler III, W., 2000. Potential role of gas hydrate decomposition in generating submarine slope failures. In: Max, M.D. (Ed.), Natural Gas Hydrate in Oceanic and Permafrost Environments. Kluwer Academic Publishers, Dordrecht, pp. 149–156.
Paull, C.K., Ussler III, W., Dallimore, S., Blasco, S., Lorenson, T., Melling, H., McLaughlin, F., Nixon, F.M., 2007. Origin of pingo-like features on the Beaufort Sea shelf and their possible relationship to decomposing methane gas hydrates. Geophys. Res. Lett. 34 https://doi.org/10.1029/2006GL027977. L01603.
Paull, C.K., Dallimore, S., Hughes-Clarke, J., Blasco, S., Lundsten, E., Ussler III, W., Graves, D., Sherman, A., Conway, K., Melling, H., Vagle, S., Collett, T., 2011. Tracking the decomposition of permafrost and gas hydrate under the shelf and slope of the Beaufort Sea. In: 7th International Conference on Gas Hydrate, paper 5581, 12 p.
Paull, C.K., Dallimore, S.R., Caress, D.W., Gwiazda, R., Melling, H., Riedel, M., Jin, Y.K., Hong, J.K., Graves, D., Sherman, A., Lundsten, E., Anderson, K., Lundsten, L., Villinger, H., Kopf, A., Johnson, S., Vrjenhoek, R., Conway, K., Neelands, P., Cote, M., 2015a. Active mud volcanoes on the continental slope of the Canadian Beaufort Sea. Geochem. Geophys. Geosyst. 16, 2797–3342. https://doi.org/10.1002/2015GC005928.
Paull, C.K., Caress, D.W., Thomas, H., Lundsten, E., Anderson, K., Gwiazda, R., Riedel, M., McGann, M., Herguera, J.C., 2015b. Seafloor geomorphic manifestations of gas venting and shallow sub-bottom gas hydrate occurrences. Geospheres 11, 491–513.
Paull, C.K., Dallimore, S., Jin, Y.K., Caress, D.W., Lundsten, E., Anderson, K., Gwiazda, R., Riedel, M., Melling, H., Duchesne, M.J., King, E.L., 2019. Submarine Permafrost Dynamics Along the Arctic Shelf Edge. American Geolphysical Union. agu.confex.com/agu/fm19/meetingapp.cgi/Paper/491053.
Pelletier, B.R., 1988. Marine science atlas of the Beaufort Sea: Geology and geophysics. Ottawa, Ontario. In: Geological Survey of Canada Miscellaneous Report 40. https://doi.org/10.4095/126940.
Piper, D.J.W., McCall, C., 2003. A synthesis of the distribution of submarine mass movements on the Eastern Canadian Margin. In: Locat, J., Mienert, J., Boisvert, L. (Eds.), Submarine Mass Movements and Their Consequences, Advances in Natural and Technological Hazards Research, Vol. 19. Springer, Dordrecht, pp. 291–298.
Pohlman, J., Lorenson, T., Hart, P., Ruppel, C., Joseph, C., Torres, M., Edwards, B., 2011. Evidence for freshwater discharge at a gas hydrate bearing seafloor mound on the Beaufort Sea continental slope. In: American Geophysical Union Fall Meeting, Abstract GC41B-0813.
Poley, D.F., 1982. A Detailed Study of a Submerged Pingo-Like-Feature in the Canadian Beaufort Sea, Arctic, Canada [MS thesis]. Dalhousie University, Halifax, Nova Scotia, 96 p.
Pope, E.L., Peter, J., Talling, P.J., Cofaigh, C.Ó., 2018. The relationship between ice sheets and submarine mass movements in the Nordic Seas during the Quaternary. Earth Sci. Rev. https://doi.org/10.1016/j.earscirev.2018.01.007.
Puzrin, A.M., Gray, T.E., Hill, A.J., 2017. Retrogressive shear band propagation and spreading failure criteria for submarine landslides. Géotechnique 67, 95–105.
Rachold, V., Grigoriev, M.N., Are, F.E., Soloman, S., Reimnitz, W., Kassens, H., Antonow, M., 2000. Coastal erosion vs riverine sediment discharge in the Arctic Shelf seas. Int. J. Earth Sci. 89, 450–460.
Rampton, V.N., 1988. Quaternary geology of the Tuktoyaktuk Coastlands, Northwest Territories. Geol. Surv. Can. Mem. 423, 98 p.
Reimnitz, E., Maurer, D.K., 1979. Effects of storm surges on the Beaufort Sea Coast, Northern Alaska. Arctic 32, 329–344. https://www.jstor.org/stable/40509007.
Riedel, M., Brent, T.A., Taylor, G., Taylor, A.E., Hong, J.-K., Jin, Y.-K., Dallimore, S.R., 2017. Evidence for gas hydrate occurrences in the Canadian Arctic Beaufort Sea within the permafrost-associated shelf and deep-water marine environments. Mar. Pet. Geol. 81, 66–78. https://doi.org/10.1016/j.marpetgeo.2016.12.027.
Rolfe, P.F., Aylmore, L.A.G., 1977. Water and salt flow through compacted clays: I. Permeability of compacted illite and montmorillonite. Soil Sci. Soc. Am. J. 41, 489–495.
Ruppel, C., 2011. Methane hydrates and contemporary climate change. Nat. Educ. Knowlegde Proj. 3 (10), 29.
Saint-Ange, F., Kuus, P., Blasco, S., Piper, D.J.W., Hughes-Clarke, J., MacKillop, K., 2014. Multiple failure styles related to shallow gas and fluid venting, upper slope Canadian Beaufort Sea, northern Canada. Mar. Geol. 355, 136–149.
Shearer, J.M., Macnab, R.F., Pelletier, B.R., Smith, T.B., 1971. Submarine pingos in the Beaufort Sea. Science 174, 816–818.
Siddiqui, Q.A., 1988. The Iperk Sequence (Plio-Pleistocene) and its ostracod assemblages in the Eastern Beaufort Sea. Dev. Paleontontol. Stratigr. 11, 533–540. https://doi.org/10.1016/S0920-5446(08)70206-1.
Solheim, A., Berg, K., Forsberg, C.F., Bryn, P., 2005. The Storegga Slide complex: repetitive large scale sliding with similar cause and development. Mar. Pet. Geol. 22, 97–107. https://doi.org/10.1016/j.marpetgeo.2004.10.013.
Sommerfield, C.K., 2006. On sediment accumulation rates and stratigraphic completeness: lessons from Holocene Ocean margins. Cont. Shelf Res. 26, 2225–2240. https://doi.org/10.1016/j.csr.2006.07.015.
Środoń, J., 1999. Nature of mixed-layer clays and mechanisms of their formation and alteration. Annu. Rev. Earth Planet. Sci. 27, 19–53.
Sun, Q., Alves, T., Xie, X., He, J., Li, W., Ni, X., Sun, Q., 2017. Free gas accumulations in basal shear zones of mass-transport deposits (Pearl River Mouth Basin, South China Sea): an important geohazard on continental slope basins. Mar. Pet. Geol. 81, 17–32. https://doi.org/10.1016/j.marpetgeo.2016.12.029.
Sutherland, B.R., Barrett, K.J., Gingras, M.K., 2015. Clay settling in fresh and salt water. Environ. Fluid Mech. 15, 147–160.
Swarzenski, P.W., Baskaran, M., Rosenbauer, R.J., Orem, W.H., 2006. Historical trace element distribution in sediments for the Mississippi River Delta. Estuar. Coasts 29 (6B), 1094–1107.
Talling, P.J., Clare, M., Urlaub, M., Pope, E., Hunt, J.E., Watt, S.F.L., 2014. Large submarine landslides on continental slopes: geohazards, methane release, and climate change. Oceanography 27 (2), 32–45. https://doi.org/10.5670/oceanog.2014.38.
Taylor, A.E., Dallimore, S.R., Hill, P.R., Issler, E.R., Blasco, S., Wright, F., 2014. Numerical model of the geothermal regime on the Beaufort Shelf, arctic Canada since the last Interglacial. J. Geophys. Res. Earth Surf. 118, 2365–2379.

Torrence, J.K., 1983. Towards a general model of quick clay development. Sedimentology 30, 547–555.
Twichell, D., Chaytor, J.D., ten Brink, U.S., Buczkowski, B., 2009. Morphology of late Quaternary submarine landslides along the U.S. Atlantic margin. Mar. Geol. 264, 4–15.
Vanneste, M., Sultan, N., Garziglia, S., Forsberg, C.F., L'Heureux, J.S., 2014. Seafloor instabilities and sediment deformation processes: the need for integrated, multi-disciplinary investigations. Mar. Geol. 352, 183–214.
Weaver, J.S., Stewart, J.M., 1982. In situ hydrates under the Beaufort Sea Shelf. In: French, H.M. (Ed.), Proceedings, Fourth Canadian Permafrost Conference. National Research Council of Canada, Ottawa, pp. 312–319.
Weaver, P.P.E., Wynn, R.B., Kenyon, N.H., Evans, J., 2000. Continental margin sedimentation, with special reference to the Northeast Atlantic margin. Sedimentology 47, 239–256.
Westbrook, G.K., Thatcher, K.E., Rohling, E.J., et al., 2009. Escape of methane gas from the seabed along the West Spitsbergen continental margin. Geophys. Res. Lett. 36 (15). L15608.
Winters, W.J., Waite, W.F., Mason, D.H., Gilbert, L.Y., Pecher, I.A., 2007. Methane gas hydrate effect on sediment acoustic and strength properties. J. Pet. Sci. Eng. 56, 127–135.
Yorath, C.J., Shearer, J., Havard, C.J., 1971. Seismic and sediment studies in the Beaufort Sea. In: Canadian Geologic Survey Paper, no. 71–1, part A, pp. 243–244.
Zhang, T., Deng, Y., Cui, Y., Lan, H., Zhang, F., 2019. Porewater salinity effect on flocculation and desiccation cracking behavior of kaolin and bentonite considering working conditions. Eng. Geol. 251, 11–23.